

RESEARCH ARTICLE | DECEMBER 13 2023

An augmented invariant-based model of the pressure Hessian tensor using a combination of physics-assisted neural networks

Deep Shikha  ; Sawan S. Sinha  



Physics of Fluids 35, 125124 (2023)

<https://doi.org/10.1063/5.0181290>



Articles You May Be Interested In

Modeling of vibrational nonequilibrium effects on pressure Hessian tensor using physics-assisted deep neural networks

Physics of Fluids (December 2024)

Velocity gradient dynamics in compressible turbulence: Characterization of pressure-Hessian tensor

Physics of Fluids (December 2013)

A physics-informed deep learning closure for Lagrangian velocity gradient evolution

Physics of Fluids (November 2023)

06 May 2025 12:07:39



Physics of Fluids

Special Topics

Open for Submissions

[Learn More](#)



An augmented invariant-based model of the pressure Hessian tensor using a combination of physics-assisted neural networks

Cite as: Phys. Fluids **35**, 125124 (2023); doi: [10.1063/5.0181290](https://doi.org/10.1063/5.0181290)

Submitted: 16 October 2023 · Accepted: 18 November 2023 ·

Published Online: 13 December 2023



View Online



Export Citation



CrossMark

Deep Shikha^{a)} and Sawan S. Sinha^{b)}

AFFILIATIONS

Department of Applied Mechanics, Indian Institute of Technology Delhi, New Delhi 110016, India

^{a)}amz207588@iitd.ac.in

^{b)} Author to whom correspondence should be addressed: sawan@am.iitd.ac.in

ABSTRACT

Modeling the velocity gradient dynamics in incompressible turbulence requires modeling two unclosed quantities: the pressure Hessian tensor and the viscous Laplacian tensor. In this work, we model the pressure Hessian tensor using a combination of two different physics-embedded deep neural networks. The first neural network is trained specifically to predict the alignment tendencies of the eigen-vectors of the pressure Hessian tensor, whereas the second neural network is trained only to predict the magnitude of the tensor. This separation of tasks allows us to define mathematically optimal and physics-informed customized loss functions separately for the two aspects (alignment and magnitude) of the tensor. Both neural networks take invariants of the velocity gradient tensor as inputs. Even though the training of the two networks is performed using direct numerical simulation database of an incompressible stationary isotropic turbulence at a particular Reynolds number, we extensively evaluate the model at different Reynolds numbers and in different kinds of flow fields. In incompressible flows, the proposed model shows significant improvements over the existing phenomenological model (the recent fluid deformation closure model or the RFD model) of the pressure Hessian tensor. While the improvements in the alignment tendencies are convincingly evident in the shapes of the probability density functions of the cosines of various angles between eigenvectors, the improvements in the prediction of the magnitude of the pressure Hessian tensor using the new model are quantifiable in the range of 28%–89% (depending on the type of the flow field) compared to the RFD model.

Published under an exclusive license by AIP Publishing. <https://doi.org/10.1063/5.0181290>

I. INTRODUCTION

An improved understanding of the velocity gradient tensor and its evolution in a turbulent flow field is deemed to be of fundamental interest. The evolution of velocity gradients is closely related to the evolution of various non-linear processes like energy cascade, intermittency, and material element deformation that characterize turbulent flows.^{1–5} There are three plausible approaches to access and examine the velocity gradient field in a turbulent flow: (i) experimental measurements, (ii) direct numerical simulations (DNS), and (iii) development of simple dynamical models to directly track the evolution of the velocity gradient tensor without calculating the Eulerian velocity field itself. Even though some experimental observations of the velocity gradients have been made in the recent past,⁶ the available database is too limited for further extensive studies. On the other hand, DNS databases have indeed been used extensively to examine various aspects of the velocity gradient field by several researchers.^{2,7–10} Despite offering

accurate information about the velocity gradient field, performing repeated DNS simulations, especially, at a high Reynolds number is expensive and time-consuming. This brings the focus to the third approach. This approach uses simple dynamical equations to model and study the evolution of velocity gradients in turbulent flow fields. Vieillefosse¹ pioneered this approach, and subsequently, several researchers^{7,8,11–14} contributed toward improving such models. The development of this approach is desirable because (i) it is computationally simpler as the governing equations are ordinary differential equations and not partial differential equations like the Navier–Stokes equations, (ii) the temporal evolution of gradients in these equations naturally follows the motion of local fluid elements allowing for a more insightful understanding of various turbulence phenomena, and finally, (iii) such models of velocity gradients can also be used directly as closure models for the so-called Lagrangian probability density functions (PDF)-based methods of turbulence computations.¹⁵

Despite having several desirable aspects, the approach of using simple dynamical models faces two major challenges: the pressure-related process (the pressure Hessian tensor) and the diffusive viscous process are mathematically unclosed and need closure modeling to arrive at a set of mathematically closed equations, which makes numerical computations viable. To achieve mathematical closure, Vieillefosse¹ retained only the isotropic part of the pressure Hessian tensor and ignored the anisotropic part of the pressure Hessian tensor. He demonstrated that owing to the Poisson's equation for pressure, the isotropic part of the pressure Hessian tensor can be computed exactly in terms of the various components of the velocity gradient tensor itself. Furthermore, he neglected the unclosed viscous diffusion process altogether. The resulting closed equation is called the *restricted Euler equation or the REE*. Martin *et al.*¹⁶ enhanced the REE by including a model for the viscous process using what the authors called the linear diffusion model (LDM). Jeong and Girimaji¹² further improved the LDM approach using the Lagrangian–Eulerian change of variables, resulting in the development of the so-called linear Lagrangian diffusion model (LLDM). Chevillard *et al.*¹³ proposed the idea of the *recent fluid deformation (RFD)* closure and developed the first model for the anisotropic part of the pressure Hessian tensor. They used the RFD approach to propose an improved model for the viscous diffusion process as well. These advancements enabled their modeled dynamical equation to not only address the finite time singularity problem of the REE model but also helped reproduce several statistical features of stationary homogeneous isotropic turbulence. Indeed, the performance of the RFD-based models has been shown to be superior to those of all the preceding phenomenological models of the velocity gradient dynamics in incompressible stationary isotropic homogeneous turbulent flow fields.

Even though the RFD model has shown superiority over the existing phenomenological models in terms of some important flow features like (i) the alignment of the eigenvectors of the pressure Hessian tensor with the vorticity vector and (ii) predicting the magnitude of the pressure Hessian tensor, the model still suffers from the following shortcomings:

1. The alignment tendencies of the eigen directions of the pressure Hessian tensor with those of the local strain-rate tensor do not show agreement with the behavior observed in various DNS databases of turbulent flows.¹⁷ Several theoretical and DNS-based studies^{4,5,18} demonstrate that these tendencies are not only quite universal in nature, but they play an important role in intensifying the energy cascade process in incompressible turbulent flows.
2. In homogeneous isotropic flow fields, the performance of the RFD model deteriorates as the Reynolds number increases.¹⁹
3. The performance of the RFD model has not been extensively evaluated in non-homogeneous turbulent flow fields.

In recent years, machine learning (ML) has emerged as a promising modeling tool in almost all research and engineering streams. Indeed, several researchers have already employed such tools to improve the performance of turbulence closure models.^{20–24} However, most of these efforts are aimed toward the Reynolds-averaged Navier–Stokes (RANS) or the large eddy simulation (LES) paradigm. Recently, Parashar *et al.*¹⁷ pioneered the employment of ML tools to model the pressure Hessian tensor. Even though their model was

demonstrated to address some of the shortcomings of the RFD model, a detailed retrospective study reveals that the model lacks the essential requirement of the invariance of the model predictions to rotations in the working coordinate system. In a particular coordinate system which is perfectly aligned with the computational domain, the model performance is found to be satisfactory. However, in any other alternate coordinate system, the performance deteriorates drastically (more on this in Secs. III C and V). Accordingly, the overarching goal of this work is to use ML tools to develop superior high-fidelity closure models for the pressure Hessian tensor in terms of the local state of the velocity gradient tensor applicable in different kinds of turbulent flow fields and over a wide range of the Reynolds number. Toward this goal, we identify the following specific objectives:

1. To propose a combination of two different physics-assisted neural networks, which can separately predict (i) the alignment tendencies of the pressure Hessian tensor relative to the local strain-rate tensor and (ii) the magnitude of the pressure Hessian tensor. This strategy of using two different neural networks to predict two different aspects of the pressure Hessian tensor allows us to identify specific loss functions, which are adequately physics-assisted and mathematically optimal. We refer to this combination of the two neural networks as the *augmented invariant-based model (AIBM)* for the pressure Hessian tensor.
2. To perform an extensive evaluation of the AIBM by comparing its predictions against the available DNS database on the one hand and with the predictions made by the RFD model (the competing phenomenological model) on the other. To convincingly demonstrate the capability of the new model and its superiority over the RFD model, evaluations are performed in different types of flow fields: stationary incompressible isotropic homogeneous turbulent flow field at different Reynolds numbers, stationary incompressible inhomogeneous turbulent field (channel flow), and compressible homogeneous decaying turbulence.

Even though the first neural network is still based on the architecture of the tensor basis neural network (TBNN) proposed by Ling *et al.*²⁴ and subsequently employed by Parashar *et al.*,¹⁷ we introduce several new physics-based features in this architecture to achieve a more robust performance of the model and to address the shortcomings of the model of Parashar *et al.*¹⁷ In combination with this, we introduce another neural network to predict the magnitude of the pressure Hessian tensor. The input parameters of this novel neural network are carefully chosen based on a DNS-based study on the behavior of the magnitude of the pressure Hessian tensor.

This paper is organized as follows: Sec. II presents a brief overview of the exact but unclosed governing equations of the velocity gradients in an incompressible flow field. In Sec. III, we present the details of the ML-assisted modeling strategy employed in this work. Section IV discusses the plan of evaluation and quantities of interest for our model. In Secs. V and VI, we present extensive evaluations of the model against DNS behavior as well as with the existing incompressible models. Section VII concludes the paper with a brief summary.

II. GOVERNING EQUATIONS OF VELOCITY GRADIENT DYNAMICS

We start with the continuity and the momentum equations for an incompressible flow field:

$$\frac{\partial V_k}{\partial x_k} = 0, \quad (1)$$

$$\frac{\partial V_i}{\partial t} + V_k \frac{\partial V_i}{\partial x_k} = -\frac{1}{\rho} \frac{\partial p}{\partial x_i} + \frac{\mu}{\rho} \frac{\partial^2 V_i}{\partial x_k \partial x_k}, \quad (2)$$

where V_i , x_i , ρ , and μ represent the velocity, spatial coordinate, density, and dynamic viscosity, respectively. After taking the spatial derivative of Eq. (2), the exact time evolution equation of the velocity gradient tensor ($A_{ij} = \frac{\partial V_i}{\partial x_j}$) can be derived:

$$\frac{DA_{ij}}{Dt} = -A_{ik}A_{kj} - \underbrace{\frac{1}{\rho} \frac{\partial^2 p}{\partial x_i \partial x_j}}_{P_{ij}} + \underbrace{\frac{\mu}{\rho} \frac{\partial^2 A_{ij}}{\partial x_k \partial x_k}}_{\gamma_{ij}}, \quad (3)$$

where P_{ij} and γ_{ij} represent the pressure Hessian and the viscous Laplacian tensors influencing the evolution of the velocity gradient tensor. The operator $\frac{D}{Dt}$ is the substantial derivative, which represents the rate of change (following the motion of a small fluid element). As evident in Eq. (3), the velocity gradient evolution is governed by three processes. The first process on the right-hand side (RHS) is the self-stretching term, and it represents the effect of inertia on the velocity gradient evolution process. The self-stretching term can be computed using the velocity gradient tensor of the current fluid element itself. In other words, it is mathematically closed. The second process on the RHS is the pressure Hessian tensor. The pressure Hessian term includes the local and nonlocal effects of pressure on the velocity gradient evolution process. It can be further decomposed into two parts,¹ the isotropic ($Z\delta_{ij}/3$) and the anisotropic (Q_{ij}),

$$P_{ij} = Z \frac{\delta_{ij}}{3} + Q_{ij}. \quad (4)$$

Following this decomposition, $Q_{ii} = 0$. Furthermore, taking the trace of Eq. (3) and following the divergence free condition ($A_{ii} = 0$), we arrive at Poisson's equation of incompressible flows:

$$\frac{1}{\rho} \frac{\partial^2 p}{\partial x_i \partial x_i} = -A_{lm}A_{ml}. \quad (5)$$

Equation (5) implies that the isotropic part of the pressure Hessian term is known exactly in terms of the second invariant ($A_{lm}A_{ml}$) of velocity gradient tensor

$$Z = -A_{lm}A_{ml}. \quad (6)$$

The third process on RHS is the viscous Laplacian term. The viscous Laplacian process involves higher derivatives of velocity gradient and, hence, is a nonlocal and mathematically unclosed term. Thus, for incompressible turbulence, closure of Eq. (3) requires models of the viscous process and the anisotropic pressure Hessian tensor (Q). In this work, we develop and validate improved models of the anisotropic part of the pressure Hessian using machine learning tools.

III. ML-BASED MODELING OF THE PRESSURE HESSIAN TENSOR

Our primary goal is to model the influence of the anisotropic pressure Hessian tensor to achieve mathematical closure for the autonomous governing equation of the velocity gradient tensor in incompressible flows [Eq. (3)]. However, from this viewpoint, it is not necessary that we model the pressure Hessian tensor in its raw form.

The self-stretching process and the pressure Hessian process appearing in the RHS of Eq. (3) can be recast in the following manner:

$$-A_{ik}A_{kj} - \frac{Z\delta_{ij}}{3} - Q_{ij} = -\varepsilon^2 \left(\frac{A_{ik}A_{kj}}{\varepsilon^2} + \frac{Z\delta_{ij}}{3\varepsilon^2} + \frac{Q_{ij}}{\varepsilon^2} \right), \quad (7)$$

where

$$\varepsilon = \sqrt{A_{ij}A_{ij}} \quad (8)$$

represents the magnitude of the instantaneous velocity gradient tensor. Since the tensor equation [Eq. (3)] already governs the evolution of ε^2 , it suffices to model the naturally normalized version of the anisotropic pressure Hessian tensor: Q/ε^2 . We use the symbol Q' to represent this normalized version

$$Q' = Q/\varepsilon^2. \quad (9)$$

Furthermore, in this work, we plan to use two different physics-assisted deep neural networks. The first neural network aims at recovering the relative orientation of the eigenvectors of the Q' tensor (relative to the eigenvectors of the local strain-rate tensor^{4,5,18}). Since the alignments of the eigenvectors of Q' are not explicitly dependent on the magnitude of the Q' , we propose the first neural network to have the self-normalized version of the Q' tensor as its output. This self-normalized version is defined as follows:

$$\hat{Q}' = \frac{Q'}{\sqrt{Q'_{mn}Q'_{mn}}}, \quad (10)$$

which implies $\hat{Q}'_{ij}\hat{Q}'_{ij} = 1$. This network is based on the basic architecture proposed by Ling *et al.*²⁴ to model the anisotropy of the Reynolds stress tensor. However, we have added several novel aspects to this modeling strategy to suit the requirements of this work. Such details are presented in Sec. III A.

The second neural network proposed in this work is designed to predict the magnitude (a scalar quantity) of the Q' tensor. We represent this magnitude by symbol ψ , such that,

$$\psi = \sqrt{Q'_{ij}Q'_{ij}}. \quad (11)$$

More details about the modeling of ψ are presented in Sec. III B. Combining the outputs from these two neural networks, we can then have the final model for the tensor Q' as follows:

$$Q' = \psi \hat{Q}'. \quad (12)$$

We refer to this combination of the two neural networks to eventually predict the Q' tensor as the *augmented invariant-based model (AIBM)*.

A. Modeling the \hat{Q}' tensor

Our model for the \hat{Q}' tensor is based on the architecture of TBNN, which has been developed by Ling *et al.*²⁴ It was originally developed in the context of modeling the anisotropy of the Reynolds stress tensor in terms of the mean velocity gradient components of a Reynolds averaged flow field. In their architecture, the input variables were the mean strain rate and rotation rate tensors (the symmetric and anti-symmetric parts of the mean velocity gradient tensor, respectively). The output variable was the anisotropy tensor of the Reynolds stress tensor.²⁵

Since the expectation from the proposed model for the $\hat{\mathbf{Q}}'$ tensor is to reproduce the known alignment behavior of its eigenvectors relative to those of the local strain-rate tensor, we first identify a locally normalized form of the velocity gradient tensor as input to this network. This normalized form is defined as follows:

$$\mathbf{a} = \frac{\mathbf{A}}{\sqrt{A_{mn}A_{mn}}}, \quad (13)$$

where \mathbf{A} is the velocity gradient tensor. Accordingly, the locally normalized form of the strain-rate and rotation-rate tensors is

$$\mathbf{s} = \frac{\mathbf{a} + \mathbf{a}^T}{2}, \quad \mathbf{w} = \frac{\mathbf{a} - \mathbf{a}^T}{2}. \quad (14)$$

We emphasize that from a modeling perspective, it is indeed desirable to have appropriately normalized versions of the input and output parameters. An apt normalization is expected to keep the quantity within some numerical bounds. In the case of neural networks, such numerical boundedness is especially helpful in avoiding large fluctuations in various weights and biases that are computed during the training process, which in turn, can lead to faster convergence of the loss function.²⁶

Following the Cayley–Hamilton theorem,²⁵ we write $\hat{\mathbf{Q}}'$ as a linear combination of ten anisotropic tensor bases ($\mathbf{T}^{(n)}$). We express $\hat{\mathbf{Q}}'$ as

$$\hat{\mathbf{Q}}' = \sum_{n=1}^{10} g^{(n)}(\lambda_1, \dots, \lambda_5) \mathbf{T}^{(n)}. \quad (15)$$

Pope *et al.*²⁵ derived the ten anisotropic tensor basis $\mathbf{T}^{(n)}$ and five independent invariants λ_i of the normalized strain rate and the normalized rotation rate tensors. For our work, the ten anisotropic basis tensors $\mathbf{T}^{(n)}$ are defined in terms of the normalized strain rate (\mathbf{s}) and rotation rate (\mathbf{w}) tensors.

$$\begin{aligned} \mathbf{T}^{(1)} &= \mathbf{s}, & \mathbf{T}^{(6)} &= \mathbf{w}^2 \mathbf{s} + \mathbf{s} \mathbf{w}^2 - \frac{2}{3} \mathbf{I} \cdot \text{Tr}(\mathbf{s} \mathbf{w}^2), \\ \mathbf{T}^{(2)} &= \mathbf{s} \mathbf{w} - \mathbf{w} \mathbf{s}, & \mathbf{T}^{(7)} &= \mathbf{w} \mathbf{s} \mathbf{w}^2 - \mathbf{w}^2 \mathbf{s} \mathbf{w}, \\ \mathbf{T}^{(3)} &= \mathbf{s}^2 - \frac{1}{3} \mathbf{I} \cdot \text{Tr}(\mathbf{s}^2), & \mathbf{T}^{(8)} &= \mathbf{s} \mathbf{w} \mathbf{s}^2 - \mathbf{s}^2 \mathbf{w} \mathbf{s}, \\ \mathbf{T}^{(4)} &= \mathbf{w}^2 - \frac{1}{3} \mathbf{I} \cdot \text{Tr}(\mathbf{w}^2), & \mathbf{T}^{(9)} &= \mathbf{w}^2 \mathbf{s}^2 + \mathbf{s}^2 \mathbf{w}^2 - \frac{2}{3} \mathbf{I} \cdot \text{Tr}(\mathbf{s}^2 \mathbf{w}^2), \\ \mathbf{T}^{(5)} &= \mathbf{w} \mathbf{s}^2 - \mathbf{s}^2 \mathbf{w}, & \mathbf{T}^{(10)} &= \mathbf{w} \mathbf{s}^2 \mathbf{w}^2 - \mathbf{w}^2 \mathbf{s}^2 \mathbf{w}. \end{aligned} \quad (16)$$

Here, \mathbf{I} represents the identity tensor of order two and Tr means the trace of the tensor. In Eq. (15), symbols $\lambda_1, \dots, \lambda_5$ represent the five invariants of the \mathbf{s} and \mathbf{w} tensors are defined as follows:

$$\lambda_1 = \text{Tr}(\mathbf{s}^2), \quad \lambda_2 = \text{Tr}(\mathbf{w}^2), \quad \lambda_3 = \text{Tr}(\mathbf{s}^3), \quad \lambda_4 = \text{Tr}(\mathbf{w}^2 \mathbf{s}), \quad \lambda_5 = \text{Tr}(\mathbf{w}^2 \mathbf{s}^2). \quad (17)$$

The symbol $g^{(n)}$ in Eq. (15) represents the ten coefficients that need to be calculated based on the tensor basis neural network. In general, all $g^{(n)}$'s are expected to have nonlinear dependence on λ_i .

In Fig. 1, we present a schematic diagram of the TBNN architecture. The architecture has two input layers. The primary input layer is the layer of tensor invariants. This layer takes the five tensor invariants ($\lambda_1, \dots, \lambda_5$) as input. The primary input layer is followed by a series of

hidden layers such that the final hidden layer gives the set of ten coefficients $g^{(n)}(\lambda_1, \dots, \lambda_5)$. The secondary input layer takes input from the ten tensor basis. The “inner product” of the final hidden layer with the second input layer gives the final output layer. The output layer gives the predicted $\hat{\mathbf{Q}}'$.

An important aspect of any neural network is to define an appropriate loss function with the help of which a desired set of physical behavior is reproduced by the model. In this work, we employ a custom loss function, which is defined based on the relative orientation of the eigenvectors of the normalized strain rate (\mathbf{s}) and those of the $\hat{\mathbf{Q}}'$ tensor. The three eigenvectors of the \mathbf{s} tensor make a set of mutually perpendicular axes. Similarly, the three eigenvectors of the $\hat{\mathbf{Q}}'$ make another set of three mutually perpendicular directions. We denote the eigenvectors of the \mathbf{s} tensor as $\hat{\mathbf{e}}_{\alpha_s}, \hat{\mathbf{e}}_{\beta_s}, \hat{\mathbf{e}}_{\gamma_s}$ corresponding to the three eigenvalues being α_s, β_s , and γ_s , where¹ $\alpha_s > \beta_s > \gamma_s$. On the other hand, we denote the eigenvectors of the $\hat{\mathbf{Q}}'$ tensor as $\hat{\mathbf{e}}_{\alpha_p}, \hat{\mathbf{e}}_{\beta_p}, \hat{\mathbf{e}}_{\gamma_p}$ with the three eigenvalues being α_p, β_p , and γ_p , where⁵ $\alpha_p > \beta_p > \gamma_p$. These eigenvectors are schematically presented in Fig. 2. We define the relative orientation of the sets of eigenvectors of the two tensors (\mathbf{s} and $\hat{\mathbf{Q}}'$) in terms of three Euler angles²⁷ (θ, ξ, η) as shown in Fig. 2. The relationship between these angles and the various eigenvectors is follows:

$$\cos \xi = \hat{\mathbf{e}}_{\gamma_s} \cdot \hat{\mathbf{e}}_{\gamma_p}, \quad \cos \theta = \hat{\mathbf{e}}_{\alpha_s} \cdot \hat{\mathbf{e}}_{\text{proj}}, \quad \cos \eta = \hat{\mathbf{e}}_{\beta_p} \cdot \hat{\mathbf{e}}_{\text{norm}}, \quad (18)$$

where

$$\hat{\mathbf{e}}_{\text{proj}} = \frac{\hat{\mathbf{e}}'_{\text{proj}}}{|\hat{\mathbf{e}}'_{\text{proj}}|}, \quad \hat{\mathbf{e}}'_{\text{proj}} = \hat{\mathbf{e}}_{\alpha_p} - (\hat{\mathbf{e}}_{\alpha_p} \cdot \hat{\mathbf{e}}_{\gamma_s}) \hat{\mathbf{e}}_{\gamma_s}, \quad \hat{\mathbf{e}}_{\text{norm}} = \hat{\mathbf{e}}_{\text{proj}} \times \hat{\mathbf{e}}_{\gamma_s}. \quad (19)$$

Here, $||$ means the magnitude of the vector in context. We wish to train the TBNN model [Eqs. (15)–(17)] such that the orientation of the set of eigenvectors of the predicted $\hat{\mathbf{Q}}'$ tensor relative to the eigenvectors of \mathbf{s} tensor (taken from DNS database) approaches toward the relative orientation of the set of eigenvectors of the $\hat{\mathbf{Q}}'$ tensor to those of the \mathbf{s} tensor as observed in turbulent flow fields (DNS database). For such a training, we define a mathematically optimal loss function (J) in terms of just three Euler angles θ, ξ , and η ,

$$\begin{aligned} J &= L_1 + L_2 + L_3, \\ L_1 &= \frac{\sum_{j=1}^m (|\cos \xi_{\text{DNS}}| - |\cos \xi_{\text{model}}|)^2_j}{\sum_{j=1}^m |\cos \xi_{\text{DNS}}|^2_j}, \\ L_2 &= \frac{\sum_{j=1}^m (|\cos \theta_{\text{DNS}}| - |\cos \theta_{\text{model}}|)^2_j}{\sum_{j=1}^m |\cos \theta_{\text{DNS}}|^2_j}, \\ L_3 &= \frac{\sum_{j=1}^m (|\cos \eta_{\text{DNS}}| - |\cos \eta_{\text{model}}|)^2_j}{\sum_{j=1}^m |\cos \eta_{\text{DNS}}|^2_j}. \end{aligned} \quad (20)$$

The loss function (J) is minimized while training the network parameters (weights, biases), where m is the number of training samples

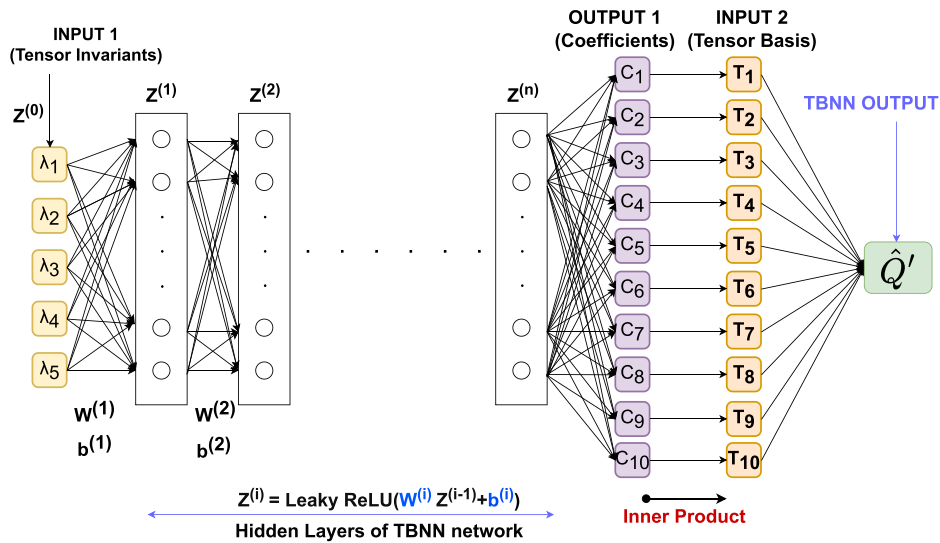


FIG. 1. A schematic diagram of the TBNN architecture for predicting \hat{Q}' .

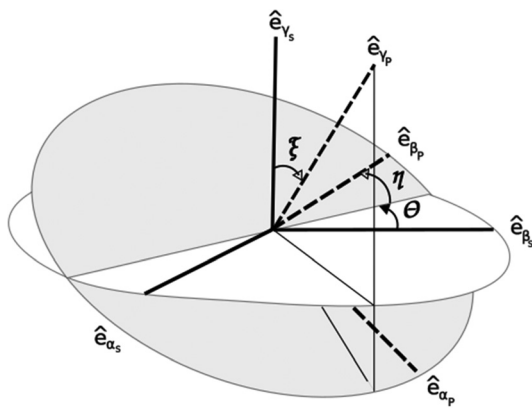


FIG. 2. The three Euler angles²⁷ (θ , ξ , and η) to describe the relative orientation of \hat{e}_{α_p} , \hat{e}_{β_p} , \hat{e}_{γ_p} with respect to \hat{e}_{α_s} , \hat{e}_{β_s} , \hat{e}_{γ_s} .

required to train the neural network. The subscript DNS implies that the quantity is sourced directly from a DNS database.

Our neural network is trained using the homogeneous isotropic incompressible²⁸ DNS data at the Taylor Reynolds number 433. We extract the velocity gradients and the pressure Hessian data at a fixed time instant when all statistics have reached their stationary states. We use a set of 250 000 total data points, from which 200 000 data points are used for training the neural network, and the remaining 50 000 data points are kept unseen to the neural network for validating the performance of the trained model at the end of completing every training cycle.

We use the Leaky rectified linear unit (Leaky ReLU) activation function between the hidden layers to introduce nonlinearity. An optimizer is required to minimize the training loss. Here, we use the Adamax optimizer²⁶ for optimizing the loss function [Eq. (20)]. In our experiments, we found that the Adamax optimizer leads to faster convergence of the loss function.

The three essential hyperparameters in training a neural network are as follows: (a) the batch size, (b) the hidden layer structure, and (c) the learning rate. To optimize the computational efforts, the mini-batch gradient descent method is used. In this method, the complete training data set is divided into mini-batches, and it updates the parameters batch-wise subsequent to getting exposed to the full batch data points. This method leads to faster convergence compared to the full-batch gradient descent. Moreover, this method leads to a smoother loss profile compared to the stochastic gradient descent method.²⁶ The third hyperparameter to tune is the learning rate. A very high learning rate may skip the global minima of the objective function. On the other hand, a very slow learning rate will increase the computational time.

To tune the neural network's hyperparameters, we use the Bayesian optimization technique.²⁹ In this technique, different sets of hyperparameter space are created from the defined objective function. It creates several different neural networks using their corresponding set of hyperparameters. These neural networks are trained, and their corresponding converged values of validation losses are calculated. An optimum set of hyperparameters is chosen based on the minimum value of the converged validation losses. Our Bayesian optimization technique found the minimum validation error for the neural network with the batch size being 16 384, the learning rate being 1×10^{-3} , and the hidden layer structure being [50, 100, 100, 100, 50].

Furthermore, we regularize our network with the use of dropout ratio³⁰ (ratio of number of nodes disregarded to the total number of nodes). We use a dropout value of 0.1. We also use an early stopping criterion on the validation loss, which stops further training of the model when no improvement is observed over the previous ten epochs. We have examined the training and the validation loss curves vs number of training epochs. The training curve and the validation curve converged at 6.398×10^{-1} and 6.668×10^{-1} , respectively. Although there is a marginal difference in loss values between the randomly initialized state of the model (untrained, epoch = 0) and the final trained model (epoch = 400), there is indeed a significant improvement in terms of all the statistics to be presented and discussed in Sec. VI. Hence, we deem this reduction in loss to be adequate for our work.

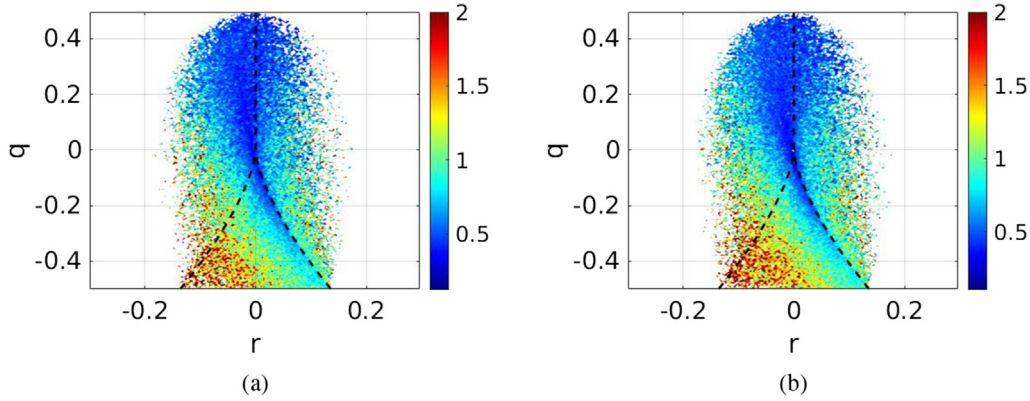


FIG. 3. Contour plot of $\langle \psi | q, r \rangle$ using: (a) isotropic turbulence data²⁸ and (b) channel flow data.³⁷

B. A new model for ψ

The first step toward developing a new neural network to predict ψ [Eq. (11)] is to identify a viable set of input arguments for the model. Since the model for ψ is expected to provide closure for the evolution equation of the velocity gradient tensor [Eq. (3)], we expect the input arguments to represent some aspects of the \mathbf{A} tensor itself. Furthermore, since ψ is a scalar quantity, we propose the input arguments to be appropriate scalars. Specifically, we propose these input scalars to be the invariants of the self-normalized velocity gradient tensor (a).

The three invariants (p , q , and r) of the self-normalized velocity gradient tensor (a) are defined as follows:

$$p \equiv -\text{Tr}[\mathbf{a}] = -\mathbf{s}_{ii}, \quad (21a)$$

$$q \equiv \frac{1}{2}(p^2 - \text{Tr}[\mathbf{a}^2]) = \frac{1}{2}(p^2 - \mathbf{s}_{ij}\mathbf{s}_{ji} - \mathbf{w}_{ij}\mathbf{w}_{ji}), \quad (21b)$$

$$r \equiv \frac{1}{3}(-p^3 + 3pq - \text{Tr}[\mathbf{a}^3]) = \frac{1}{3}(-p^3 + 3pq - \mathbf{s}_{ij}\mathbf{s}_{jk}\mathbf{s}_{ki} - 3\mathbf{w}_{ij}\mathbf{w}_{jk}\mathbf{s}_{ki}), \quad (21c)$$

where \mathbf{s} and \mathbf{w} represent the normalized strain rate and rotation rate tensors, respectively [Eq. (14)]. In incompressible flows, p being the trace of the velocity gradient tensor is identically zero (following the continuity equation). Thus, among the three invariants of \mathbf{a} , only q and r are of modeling significance.

There are several reasons with which we justify our choice of using q and r as input arguments for modeling ψ . The invariants q and r are algebraically bounded by their known limits of $[-0.5, 1]$ and $[-\sqrt{3}/9, \sqrt{3}/9]$, respectively.⁹ Furthermore, Chong³¹ shows that the invariants of velocity gradient tensor are of profound physical importance. The values of these invariants actually determine the nature of eigenvalues (real/imaginary/positive/negative) of the local state of the velocity gradient tensor. The nature of eigenvalues, in turn, determines the pattern of local streamlines (deformation pattern of local fluid elements).

Several DNS-based studies of a variety of flow fields have reported near-universal behavior of several turbulence statistics when they are observed in terms of these invariants.^{2,9,32–36} To further support the suitability of q and r as input arguments for modeling ψ , we examine the variation in ψ directly in terms of q and r using the DNS

database of two different types of turbulent flows: stationary isotropic turbulence²⁸ and channel flow.³⁷ We have computed the averaged value of ψ conditioned upon q and r : $\langle \psi | q, r \rangle$. We present the contours of $\langle \psi | q, r \rangle$ over the $q - r$ space in Fig. 3. Figure 3(a) shows statistics using the DNS data of incompressible stationary isotropic turbulence.²⁸ Figure 3(b) shows contours of $\langle \psi | q, r \rangle$ using the DNS data of a channel flow simulation.³⁷ We observe that the pattern of contours of $\langle \psi | q, r \rangle$ in Figs. 3(a) and 3(b) is quite similar. This suggests that irrespective of the type of flow fields (at least for the types considered in this work), the functional dependence of ψ on q and r is very similar despite the flow fields being very different from each other. Furthermore, we observe that except for the region in the lower-left quadrant, the order of magnitude of $\langle \psi | q, r \rangle$ in other regions is close to unity. Indeed, this is a desirable feature of the to-be-modeled variable from the viewpoint of training a neural network.

In Fig. 4, we present the contours of the joint probability density function of q and r from the two flow fields. We observe that in both flow fields, the population of fluid particles is distributed in the same universal pattern (tear-drop shape) as observed in many other types of flow fields.^{2,9,32–36} The bulk of the fluid particles are concentrated either in the top-left quadrant or in the right-bottom quadrant along the Vieillefosse curve.¹ Comparing these distributions with the contours of $\langle \psi | q, r \rangle$ in Fig. 3, it becomes clear that even though the $\langle \psi | q, r \rangle$ tends to be high in the left-bottom region, the probability of realization of such sets of (q, r) itself is not significant.

Having identified the input arguments, we propose a fully connected neural network to predict ψ in terms of q and r . In Fig. 5, we present a schematic diagram of this model. The input layer is followed by a series of hidden layers. The neural network output layer gives the normalized magnitude of the anisotropic part of the pressure Hessian tensor (ψ).

The neural network is trained using the incompressible isotropic turbulence DNS data²⁸ Reynolds number of 433 (based on the Taylor microscale). Like the first neural network, we used 200 000 data points for training the neural network and 50 000 data points for cross-validating the neural network performance at the end of every training epoch. The objective function (J) of this neural network (Fig. 5) is defined as the relative mean square error (RMSE)

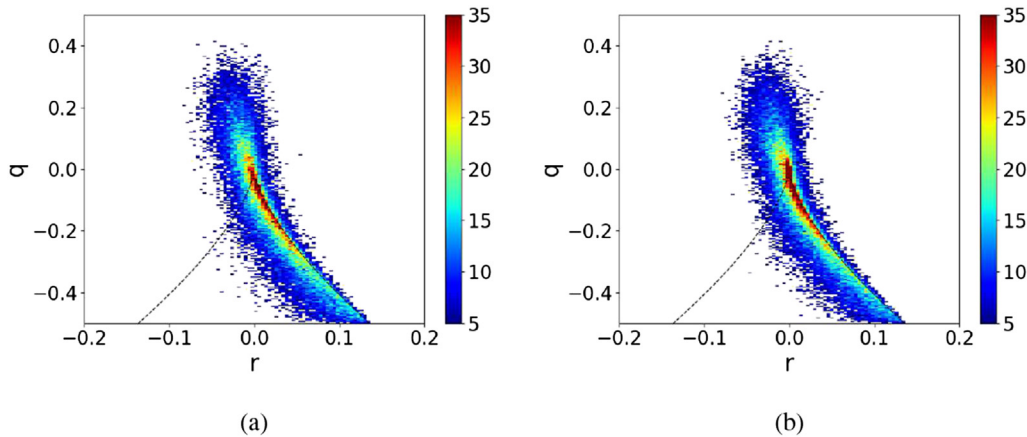


FIG. 4. Joint-PDF of q and r using: (a) isotropic turbulence data²⁸ and (b) channel flow data.³⁷

$$J = \frac{\sum_{j=1}^m (\psi_{DNS} - \psi_{model})_j^2}{\sum_{j=1}^m (\psi_{DNS})_j^2}, \quad (22)$$

where m is the number of training examples required to train the neural network.

We find an optimum set of hyperparameters using the Bayesian optimization technique, which converged to the minimum validation error with a neural network having its batch size as 4096, its learning rate being 5×10^{-3} , and its hidden layer structure being [50, 80, 50]. We use the Leaky ReLU as the activation function and Adamax as the loss function optimizer. Furthermore, we used a dropout ratio of 0.1 and an early stopping criterion of 20 epochs. The training and validation loss curves of the neural network are converged at 4.38×10^{-1} and 7.87×10^{-1} , respectively.

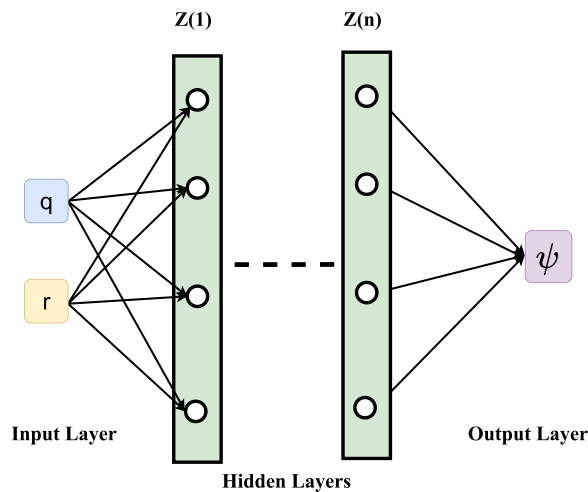


FIG. 5. A schematic diagram of the neural network architecture for predicting ψ [Eq. (11)].

The combination of two neural networks developed in Secs. III A and III B is proposed to predict the \mathbf{Q}' tensor. We refer to this combination as the *augmented invariant-based model* (AIBM). In Fig. 6, we present a summarizing schematic of this model. The overall inputs for this combined model are the locally normalized strain-rate and rotation-rate tensors (\mathbf{s} and \mathbf{w}). The first neural network extracts the five invariants mentioned in Eq. (17) as its first input layer to proceed, whereas the second neural network extracts the invariants q and r [Eqs. (21a)–(21c)] as its input. The outputs of the AIBM model (ψ and $\hat{\mathbf{Q}}'$) eventually predict \mathbf{Q}' in accordance with Eq. (12).

C. Augmentations in the AIBM compared to the existing ML model

As mentioned in the introduction, this work attempts to improve the existing ML-based model for the pressure Hessian tensor proposed by Parashar *et al.*¹⁷ Accordingly, the AIBM has been proposed. However, before we proceed to evaluate the new model in the next

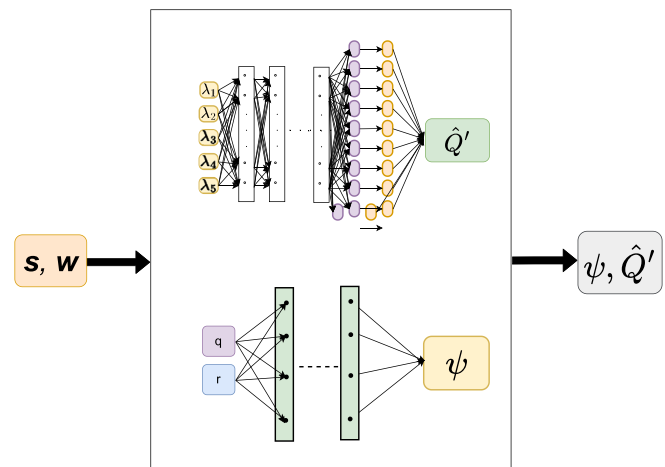


FIG. 6. A schematic diagram of new model: the augmented invariant-based model (AIBM).

section, here we present a summary highlighting the similarities and the differences between the AIBM and the model of Parashar *et al.*¹⁷

Both models do employ the TBNN architecture of Ling *et al.*²⁴ to predict some aspects of the pressure Hessian tensor. However, there are important differences in the implementation of TBNN in the two models. While AIBM employs TBNN to predict only the alignment aspects (eigenvectors) of the anisotropic pressure Hessian tensor and uses another specialized network to predict the magnitude of the tensor, the model of Parashar *et al.*¹⁷ is entirely based on the TBNN alone to predict a globally normalized version of the anisotropic pressure Hessian tensor. This globally normalized version is defined by Parashar *et al.*¹⁷ as $\frac{\mathbf{Q}}{\langle A_{mn}A_{mn} \rangle_{\text{volume}}}$, where $\langle A_{mn}A_{mn} \rangle_{\text{volume}}$ is the volume averaged value (averaged over the entire computational domain of the DNS database used for training the model) of the square of the magnitude of \mathbf{A} tensor.

Furthermore, to achieve better alignment predictions of the anisotropic pressure Hessian tensor, the model of Parashar *et al.*¹⁷ modified the original tensor basis [Eq. (16)] using what they called as the *min-max normalization* of the tensor basis elements. They redefined all nine components of each tensor basis [Eq. (16)] as

$$T'_{ij} = \frac{T_{ij} - T_{ij}^{\min}}{T_{ij}^{\max} - T_{ij}^{\min}}, \quad (23)$$

where T_{ij}^{\min} and T_{ij}^{\max} are the global (volume averaged over the entire computational domain of DNS database used for training the model) minimum and maximum values of the corresponding tensor basis element T_{ij} [Eq. (16)]. In Eq. (23), the symbols T'_{ij} s are the modified counterparts of T_{ij} s. Even though this min-max normalization led to better predictions of the eigenvectors of the modeled pressure Hessian tensor in a coordinate system that was aligned with the flow domain (a periodic box of homogeneous isotropic turbulence), a retrospective analysis actually reveals that this modification [Eq. (23)] violates the rotational invariance of the predicted pressure Hessian tensor. Unlike Parashar *et al.*,¹⁷ the AIBM retains the original form of the basis tensors in Eq. (16) and is thus guaranteed to retain the rotational invariance of the predicted tensor. Furthermore, the second part (Fig. 6) of the AIBM, which has been added to predict ψ , is also guaranteed to retain rotational invariance because (i) the output of this network is a scalar, and (ii) the inputs are already based on the invariants of the velocity gradient tensor (q and r).

Another important change introduced in AIBM is the use of loss functions, which are not only mathematically more optimal but also physically more sensible as compared to the loss function used by Parashar *et al.*¹⁷ Since the role of TBNN in AIBM is to specifically target the orientations of the eigenvectors of the anisotropic pressure Hessian tensor relative to the local strain-rate tensor, we have used a minimum number of parameters (merely the three Euler angles, Fig. 2) to define the loss function. Furthermore, by definition, this loss function is independent of the choice of the working coordinate system. In contrast, Parashar *et al.*¹⁷ employed a loss function, which is based on matching all the nine individual components of the predicted tensor to the corresponding components sourced from the DNS database. They defined the loss function as follows:

$$J = \frac{1}{2mn} \sum_{j=1}^m \sum_{i=1}^3 \sum_{k=1}^3 \left[\left(\frac{Q_{ik}}{\langle A_{mn}A_{mn} \rangle_{\text{volume}}} \right)^{\text{model}} - \left(\frac{Q_{ik}}{\langle A_{mn}A_{mn} \rangle_{\text{volume}}} \right)^{\text{DNS}} \right]^2, \quad (24)$$

where m is the number of training sample points required to train the neural network, and $n=9$. Not only is this loss function [Eq. (24)] over-constrained (as far as recovering the alignment tendencies of the eigenvectors are concerned), it is inherently dependent on the specific choice of the working coordinate system.

D. Calculation methods of the AIB and RFD models

The nine components of the self-normalized components of the velocity gradient tensor (\mathbf{a}) [Eq. (13)] are the inputs to the AIB model. The subsequent calculation steps of the AIB model are as follows:

1. Compute the scalar components of \mathbf{s} and \mathbf{w} using Eq. (14).
2. Compute the five invariants λ_1 to λ_5 using Eq. (17).
3. Using λ_1 to λ_5 and the embedded first neural network (Fig. 1), compute the ten coefficients (g_i 's).
4. Compute the ten basis tensors $\mathbf{T}^{(1)}$ to $\mathbf{T}^{(10)}$ using Eq. (16).
5. Assemble together the computed g_i 's and the basis tensors $\mathbf{T}^{(i)}$'s, compute the $\hat{\mathbf{Q}}$ in accordance with Eq. (15).
6. To compute the magnitude of the pressure Hessian tensor, use Eqs. (21a)–(21c) to first find the invariants q and r (p is trivially zero in incompressible flow fields).
7. Using the computed q and r , the second neural network (Fig. 5) is invoked to find the value of ψ . Using this value of ψ and the $\hat{\mathbf{Q}}$ tensor already calculated in step 5, finally compute the full normalized anisotropic pressure Hessian tensor (\mathbf{Q}') in accordance with Eq. (12).

Quite differently, the RFD model of Chevillard *et al.*¹⁹ models the pressure Hessian tensor as

$$P_{ij}^{\text{RFD}} = C_{ij}^{-1} \frac{A_{lm}A_{ml}}{C_{pp}^{-1}}, \quad (25)$$

where \mathbf{A} is the local velocity gradient tensor. The symbol \mathbf{C} is called the *recent Cauchy–Green* tensor and has been proposed by the authors¹⁹ as an approximation for the exact exponential evolution of the Cauchy–Green tensor. The matrix \mathbf{C} in Eq. (25) is computed using the following matrix exponential:

$$\mathbf{C} = e^{\tau_K \mathbf{A}} e^{\tau_K \mathbf{A}^T}, \quad (26)$$

where τ_K is the Kolmogorov timescale described as

$$\tau_K = \sqrt{\frac{\nu}{\mathcal{E}}}. \quad (27)$$

The symbols ν and \mathcal{E} are the kinematic viscosity and the dissipation rate of turbulence kinetic energy, respectively.

Using a selected state of the velocity gradient tensor (\mathbf{A}) from a reference DNS database, Eq. (25) is first used to find the \mathbf{P} tensor using the RFD model. The isotropic part is then subtracted out to arrive at the anisotropic part of the tensor

$$\mathbf{Q}_{ij}^{\text{RFD}} = P_{ij}^{\text{RFD}} - P_{nn}^{\text{RFD}} \frac{\delta_{ij}}{3} = C_{ij}^{-1} \frac{A_{lm}A_{ml}}{C_{pp}^{-1}} - C_{nn}^{-1} \frac{A_{lm}A_{ml}}{C_{pp}^{-1}} \frac{\delta_{ij}}{3}. \quad (28)$$

The tensor components thus obtained are then normalized by the magnitude of the velocity gradient tensor [Eq. (9)] to arrive at the components of \mathbf{Q}' predicted by the RFD model

$$Q_{ij}^{RFD} = \frac{Q_{ij}^{RFD}}{\varepsilon^2}. \quad (29)$$

IV. PLAN OF EVALUATION AND QUANTITIES OF INTEREST

The performance of the new model is evaluated by comparing its predictions against the pertinent behavior observed in direct numerical simulations of various kinds of turbulent flow fields. Furthermore, to understand the advantages/disadvantages of AIBM compared to other existing models, comparisons are made with the predictions of the model of Parashar *et al.*¹⁷ and that the recent fluid deformation closure (RFD) model of Chevillard *et al.*¹³ The comparison with the model of Parashar *et al.*¹⁷ is presented in Sec. V. The detailed comparisons of AIBM-based predictions against DNS and the RFD behavior are presented in Sec. VI.

Our aim is to develop a model robust enough to predict the statistics of \mathbf{Q}' tensor in a variety of flow fields with different Reynolds numbers. We perform the training of the model using a part of the flow field extracted from a direct numerical simulation of an incompressible stationary isotropic turbulent flow at the Reynolds number (based on Taylor micro-scale) of 433. This data set has been sourced from the John Hopkins University turbulence database (JHTD).²⁸ After the trained model has been obtained, we evaluate the model by comparing the model predictions against the behavior observed in DNS database of various turbulent flow fields. In Table I, we present descriptions of these flow fields. In Table I, Re_λ represents the Reynolds number based on Taylor microscale,³⁸ Re_τ represents the friction Reynolds number,³⁹ and M_T represents the turbulent Mach number.^{8,9} While sources I and II are of incompressible stationary isotropic turbulence at different Reynolds numbers, source III is a turbulent channel flow. Finally, source IV is a compressible isotropic decaying turbulent flow field. All these sources are deemed to be reliable and have been cited earlier by various other researchers (source I,^{22,40} source II,^{41,42} source III,^{22,23} and source IV^{8,9}).

From every DNS data set (mentioned in Table I), we extract various velocity gradient and the pressure gradient scalar components to find the \mathbf{A} and \mathbf{Q} tensors. Subsequently, exactly \mathbf{a} , \mathbf{s} , \mathbf{w} , q , r , $\hat{\mathbf{Q}}'$, and ψ are calculated. We extract a sample of 200 000 data points from each DNS database for evaluation. To obtain predictions from various considered models (AIBM, RFD, or the model of Parashar *et al.*¹⁷), only the \mathbf{s} , \mathbf{w} tensors are sourced from the corresponding DNS dataset, and these are used as inputs for the considered models. The predicted anisotropic pressure Hessian tensors are then used for comparisons and evaluations.

We first evaluate the performance of the AIB model in terms of the alignment tendencies of the eigenvectors of $\hat{\mathbf{Q}}'$ relative to those of the local strain rate tensor (\mathbf{s}). The eigenvalues of \mathbf{s} tensor are

computed and labeled as $\alpha_s, \beta_s, \gamma_s$ such that $\alpha_s > \beta_s > \gamma_s$. The corresponding eigenvectors are labeled as $\hat{\mathbf{e}}_{\alpha_s}, \hat{\mathbf{e}}_{\beta_s}, \hat{\mathbf{e}}_{\gamma_s}$. Subsequently, the eigenvalues of $\hat{\mathbf{Q}}'$ tensor are labeled as $\alpha_p, \beta_p, \gamma_p$ such that $\alpha_p > \beta_p > \gamma_p$.¹³ The corresponding eigenvectors are labeled as $\hat{\mathbf{e}}_{\alpha_p}, \hat{\mathbf{e}}_{\beta_p}, \hat{\mathbf{e}}_{\gamma_p}$. Subsequently, the probability density functions (PDF) of the cosines of the angles existing between the eigenvectors of the strain rate tensor on one hand and the eigenvectors of the pressure Hessian tensors on the other hand are computed. We examine these PDFs to gauge the extent to which the behavior of the AIBM-predicted $\hat{\mathbf{Q}}'$ tensor agrees with the behavior of the $\hat{\mathbf{Q}}'$ tensor existing in the DNS database.

Furthermore, Ohkitani and co-workers⁴⁵ demonstrate that in incompressible turbulence, the alignment tendencies of the eigenvectors of the pressure Hessian tensor with the local vorticity vector, too, are instrumental in the cascading process. Accordingly, several previous works, both for model evaluation^{7,8,17} and in DNS-based investigations,¹⁸ have examined the orientation of the local vorticity vector with the eigenvectors of the pressure Hessian tensor. The normalized vorticity vector (ω) is extracted from the normalized rotation rate tensor (\mathbf{w}) [Eq. (14)],

$$\omega_i \equiv \frac{\varepsilon_{ijk} w_{jk}}{2}, \quad (30)$$

where ε_{ijk} represents the components of Levi-Civita tensor. Thus, we evaluate the model performance by examining the PDFs of the cosines of the angles between the vorticity vector and the three eigenvectors of $\hat{\mathbf{Q}}'$, as well.

To evaluate the performance of AIBM in terms of ψ [Eq. (11)], we examine the PDF of ψ obtained from the models and the computed directly using a DNS database. Furthermore, Chevillard *et al.*¹³ have earlier evaluated the performance of their RFD model in terms of another quantity related to the magnitude of the pressure Hessian tensor. They examined the variation of a quantity ϕ , where

$$\phi = \langle Q_{mn} Q_{mn} | q\varepsilon^2 \rangle \frac{\sigma_{q\varepsilon^2}}{\sigma_{Q_{mn} Q_{mn}}}. \quad (31)$$

The quantity ϕ is the average of the magnitude of the anisotropic pressure Hessian tensor conditioned upon the value of the second invariant of the raw velocity gradient tensor (\mathbf{A}). Using the symbols already employed in our work so far, the second invariant of \mathbf{A} indeed equals $q\varepsilon^2$ [Eq. (21b)]. Furthermore, the normalization factors $\sigma_{q\varepsilon^2}$ and $\sigma_{Q_{mn} Q_{mn}}$ in Eq. (31) represent the standard deviations of the $q\varepsilon^2$ and $Q_{mn} Q_{mn}$, respectively, computed over the considered sample. Examining the variation of ϕ with respect to the second invariant ($q\varepsilon^2$) of the dimensional velocity gradient tensor (\mathbf{A}) allows us to examine the magnitude of the anisotropic pressure Hessian tensor, especially at small values of $q\varepsilon^2$. The behavior of the magnitude of the

TABLE I. Various sources of DNS data employed for model evaluation.

Source	Type of flow field	Flow description
I	Incompressible isotropic stationary Turbulence ²⁸	$Re_\lambda = 433$
II	Incompressible isotropic stationary turbulence ⁴³	$Re_\lambda = 315$
III	Incompressible channel flow ³⁷	$Re_\tau = 1000$
IV	Compressible isotropic decaying turbulence ⁴⁴	$Re_\lambda = 55.6$ and $M_T = 1.2$

isotropic part and that of the isotropic part of the pressure Hessian tensor have a fundamental difference as locations, where qe^2 is small. The isotropic part of the pressure Hessian tensor [Eq. (6)] is expressed in terms of qe^2 as

$$Z = -A_{lm}A_{ml} = -qe^2. \quad (32)$$

Clearly as qe^2 vanishes, the isotropic part of the pressure Hessian also vanishes. However, it is a well-known behavior (observed in direct numerical simulations of incompressible turbulence) that, unlike the magnitude of Z [Eq. (32)], the magnitude of the anisotropic part does not vanish at small qe^2 values. Chevillard *et al.*¹³ emphasize that any viable model of the anisotropic pressure Hessian tensor must capture this essential behavior in the incompressible pressure Hessian field. Accordingly, in Sec. VI, we do evaluate the performance of the AIBM in terms of ϕ [Eq. (31)], as well.

V. COMPARISON WITH THE EXISTING ML-BASED MODEL

We first evaluate AIBM in comparison with the model of Parashar *et al.*¹⁷ This evaluation is performed to contrast the two models in terms of the invariance of the predicted tensor when the working coordinate system is rotated. A tensor of any order must remain invariant when the working coordinate system is rotated.

For this comparison, we identify two coordinate systems as shown in Fig. 7. The X, Y, Z coordinate system has its basis unit vectors $\hat{i}, \hat{j}, \hat{k}$ perfectly aligned with the boundaries of a cuboidal computation domain, which is employed for simulating isotropic turbulence.²⁸ The other coordinate system X^r, Y^r, Z^r has its unit vectors $\hat{i}^r, \hat{j}^r, \hat{k}^r$ such that the angle between \hat{i}^r and \hat{i} is 30° and $\hat{k}^r = \hat{k}$. If \mathbf{M} represents a second-order tensor, then M_{ij} represents the $(ij)^{th}$ component of \mathbf{M} in X, Y, Z coordinate system, whereas M_{ij}^r represents the $(ij)^{th}$ scalar component of \mathbf{M} in the X^r, Y^r, Z^r coordinate system. It is a necessary requirement of a viable model to predict the scalar components the tensor \mathbf{M} tensor, ensuring that the principal invariants of \mathbf{M} computed using M_{ij} s must be identical to the principal invariants computed using M_{ij}^r s.

The three principal invariants of \mathbf{M} are defined as follows:

$$\begin{aligned} I_1 &= e_1 + e_2 + e_3, \\ I_2 &= e_1 e_2 + e_2 e_3 + e_1 e_3, \\ I_3 &= e_1 e_2 e_3, \end{aligned} \quad (33)$$

where e_1, e_2, e_3 are the three eigenvalues of the \mathbf{M} tensor. The eigenvalues e_1, e_2, e_3 , in turn, have to be calculated by solving the characteristic equation

$$\begin{bmatrix} M_{11} & M_{12} & M_{13} \\ M_{21} & M_{22} & M_{23} \\ M_{31} & M_{32} & M_{33} \end{bmatrix} - \begin{bmatrix} e & 0 & 0 \\ 0 & e & 0 \\ 0 & 0 & e \end{bmatrix} = 0. \quad (34)$$

Using the predicted components M_{ij}^r (when the working coordinate system is X^r, Y^r, Z^r), then three eigenvalues are to be found by solving the characteristic equation

$$\begin{bmatrix} M_{11}^r & M_{12}^r & M_{13}^r \\ M_{21}^r & M_{22}^r & M_{23}^r \\ M_{31}^r & M_{32}^r & M_{33}^r \end{bmatrix} - \begin{bmatrix} e^r & 0 & 0 \\ 0 & e^r & 0 \\ 0 & 0 & e^r \end{bmatrix} = 0. \quad (35)$$

The corresponding invariants are thus obtained as

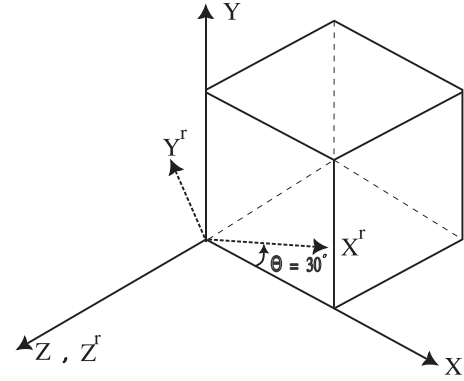


FIG. 7. The orientation of two coordinate systems with respect to a cuboidal computational domain.

$$\begin{aligned} I_1^r &= e_1^r + e_2^r + e_3^r, \\ I_2^r &= e_1^r e_2^r + e_2^r e_3^r + e_1^r e_3^r, \\ I_3^r &= e_1^r e_2^r e_3^r, \end{aligned} \quad (36)$$

where e_1^r, e_2^r, e_3^r are the three eigenvalues of \mathbf{M} computed in the rotated coordinate system. Using Eqs. (33) and (36), we define three ratios

$$F_1 = I_1^r/I_1, \quad F_2 = I_2^r/I_2, \quad F_3 = I_3^r/I_3. \quad (37)$$

If the model predicting the scalar components of \mathbf{M} is truly invariant to rotation of the coordinate system, F_1, F_2 , and F_3 must all be identically unity.

In Fig. 8(a), we plot the PDFs of F_1, F_2, F_3 obtained with the predicted $\frac{Q_{ij}}{\langle A_{mn}A_{mn} \rangle_{\text{volume}}}$ components, and the $\frac{Q_{ij}^r}{\langle A_{mn}^r A_{mn}^r \rangle_{\text{volume}}}$ components employing the model of Parashar *et al.*¹⁷ for a set of 200 000 particles using input from DNS database of source I (Table I). We observe that none of the ratios (F_1, F_2 , and F_3) shows Dirac delta distribution at 1. Moreover, the PDF distributions of the F_2 and F_3 show two peaks nearby 1.2 and 6. The second peak at 6 shows the significant probability of the invariant ratios having values greater than or equal to 6. The behavior of the PDFs in Fig. 8(a) leads to the clear conclusion that the Parashar *et al.*¹⁷ model violates the property of rotational invariance. Violation of the property of rotational invariance can lead to significant deterioration in the model performance in the case of actual flow fields as discussed by Ling *et al.*⁴⁵ In Fig. 8(b), we present the PDFs of F_1, F_2, F_3 using the AIBM model. Evidently, the PDF distributions of all the three ratios (F_1, F_2 , and F_3) are Dirac delta distributions centered at 1. This demonstrates that the AIBM model keeps the predicted tensor unchanged even when the working coordinate system is rotated. Given the demonstrated shortcomings of the model of Parashar *et al.*¹⁷ we do not perform further comparisons of AIBM with that model. Furthermore, evaluations of AIBM involve performing comparisons with (i) DNS behavior, and (ii) the RFD model behavior.

VI. COMPARISONS AGAINST DNS AND THE RFD MODEL

In this section, we present detailed evaluations of AIBM based on various quantities of interest (identified in Sec. IV). We compare AIBM against the DNS databases mentioned in Table I. Comparisons are also made with the pressure Hessian tensor predicted by the RFD

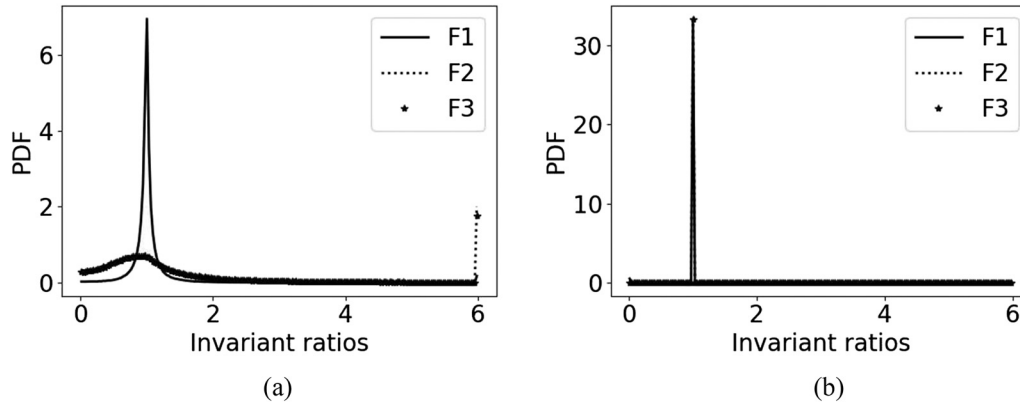


FIG. 8. PDF of invariant ratio (F_1 , F_2 , F_3) [Eq. (37)], computed from: (a) model of Parashar *et al.*¹⁷ and (b) the AIB model.

model of Chevillard *et al.*¹³ To extract the \mathbf{Q}' tensor using the RFD model, the velocity gradient tensor is taken directly from the DNS database. The RFD model provides the full-pressure Hessian tensor. However, we separate out the anisotropic part of the pressure Hessian tensor by removing the trace from the full tensor.

A. Incompressible isotropic turbulence

In this subsection, we evaluate the performance of AIBM in incompressible stationary isotropic turbulence flow field at two different Reynolds numbers (based on the Taylor microscale, Re_λ) of 433 and 315 (sources I and II, respectively). Figure 9 presents PDFs of the cosines of the angle between the eigenvectors of \mathbf{s} and \mathbf{Q}' . In each subfigure, there are three curves (DNS, AIBM, and RFD). In Figs. 9(a)–9(c), we present the PDFs of the direction cosines between the $\hat{\mathbf{e}}_{\gamma_s}$ eigenvector of the strain-rate tensor and the three eigenvectors of the pressure Hessian tensor ($\hat{\mathbf{e}}_{\alpha_p}$, $\hat{\mathbf{e}}_{\beta_p}$, $\hat{\mathbf{e}}_{\gamma_p}$), respectively. In Figs. 9(d)–9(f), we present the PDFs of the direction cosines between the $\hat{\mathbf{e}}_{\beta_s}$ eigenvector of the strain-rate tensor and the three eigenvectors of the pressure Hessian tensor ($\hat{\mathbf{e}}_{\alpha_p}$, $\hat{\mathbf{e}}_{\beta_p}$, $\hat{\mathbf{e}}_{\gamma_p}$). Similarly, in Figs. 9(g)–9(i), we present the PDFs of the direction cosines between the $\hat{\mathbf{e}}_{\alpha_s}$ eigenvector of the strain-rate tensor and the three eigenvectors of the pressure Hessian tensor ($\hat{\mathbf{e}}_{\alpha_p}$, $\hat{\mathbf{e}}_{\beta_p}$, $\hat{\mathbf{e}}_{\gamma_p}$). Examination of such alignments in homogeneous isotropic turbulence has also been performed earlier by Kalelkar¹⁸ (a DNS-based study).

The DNS results show the tendency of the $\hat{\mathbf{e}}_{\gamma_p}$ eigenvector to be aligned at 45° (the PDF curve peaking in the vicinity of 0.7) to the $\hat{\mathbf{e}}_{\gamma_s}$ eigenvector. It also shows the tendency of the $\hat{\mathbf{e}}_{\alpha_p}$ eigenvector to be parallel or anti-parallel to the eigenvector $\hat{\mathbf{e}}_{\beta_s}$ (PDF peaking in the vicinity of 1) and the $\hat{\mathbf{e}}_{\gamma_p}$ eigenvector to be orthogonal to the $\hat{\mathbf{e}}_{\beta_s}$ eigenvector. A visual comparison of the results from the RFD model and those from the DNS database clearly shows that the RFD model behavior is substantially different from the DNS behavior. The RFD model misses almost all the essential features of the DNS data alignment statistics. On the other hand, all these features of the DNS alignment statistics are captured well by AIBM. Though some of the AIBM-based predictions of the alignments PDFs show peaks with higher magnitude than

the DNS peaks, the overall performance of AIBM is significantly better than that of the RFD model.

In Fig. 10, we show the alignments of the eigenvectors ($\hat{\mathbf{e}}_{\alpha_p}$, $\hat{\mathbf{e}}_{\beta_p}$, $\hat{\mathbf{e}}_{\gamma_p}$) of \mathbf{Q}' tensor with the local vorticity vector (ω). It is known that in DNS, the vorticity vector aligns with the intermediate eigenvector of the pressure Hessian tensor.² Based on the DNS results, we observe that the vorticity vector shows a high tendency to align with the intermediate eigenvector ($\hat{\mathbf{e}}_{\beta_p}$). Furthermore, the probability density function (PDF) of the cosine of the angle between the $\hat{\mathbf{e}}_{\gamma_p}$ eigenvector and the vorticity vector has two peaks at 0 and 1, which show high tendencies of the eigenvector to align along or to be orthogonal with the vorticity vector. The third eigenvector $\hat{\mathbf{e}}_{\alpha_p}$ shows a peak at 0 and hence tends to align orthogonally with the vorticity vector. In the same figure, we also present the alignments using the RFD model and the AIBM. We observe that both the models do recover the essential expectation that the vorticity vector is a common eigenvector for the local strain rate and the pressure Hessian tensor⁴ as both AIBM and RFD capture the tendency of the vorticity vector to be aligned with the eigenvector $\hat{\mathbf{e}}_{\beta_p}$. These models also capture the alignment tendencies of the vorticity vector to be orthogonal with the other two eigenvectors $\hat{\mathbf{e}}_{\alpha_p}$, $\hat{\mathbf{e}}_{\gamma_p}$. Both the models show higher magnitudes of their PDF peaks (at 0 and 1) than the DNS curve peaks. However, the RFD model completely misses the tendency of the second peak in $\hat{\mathbf{e}}_{\gamma_p}$ alignment at 1. In contrast, the AIBM still shows a small peak at 1. Overall, in terms of vorticity alignment, we conclude that the performance of AIBM is similar to the RFD model.

Having examined the orientational aspects of the \mathbf{Q}' tensor, we now examine the AIBM performance in terms of ψ [Eq. (11)]. In Fig. 11, we present the PDF of ψ using the DNS results of source I. In the same figure, we have included the results of AIBM and the RFD models, too. We observe that the DNS curve has a wide range (0,29); however, the probability of $\psi > 8$ is nearly zero. Furthermore, the DNS plot shows a single peak at $\psi = 0.31$. The AIBM captures the width of the DNS distribution reasonably well and has a peak at $\psi = 0.41$. Furthermore, the PDF values at the respective peaks in the case of AIBM and the DNS data are almost the same (close to 1.5). In contrast to that, the RFD model shows its PDF peak with a higher magnitude (greater than 3.5), which is quite different from the

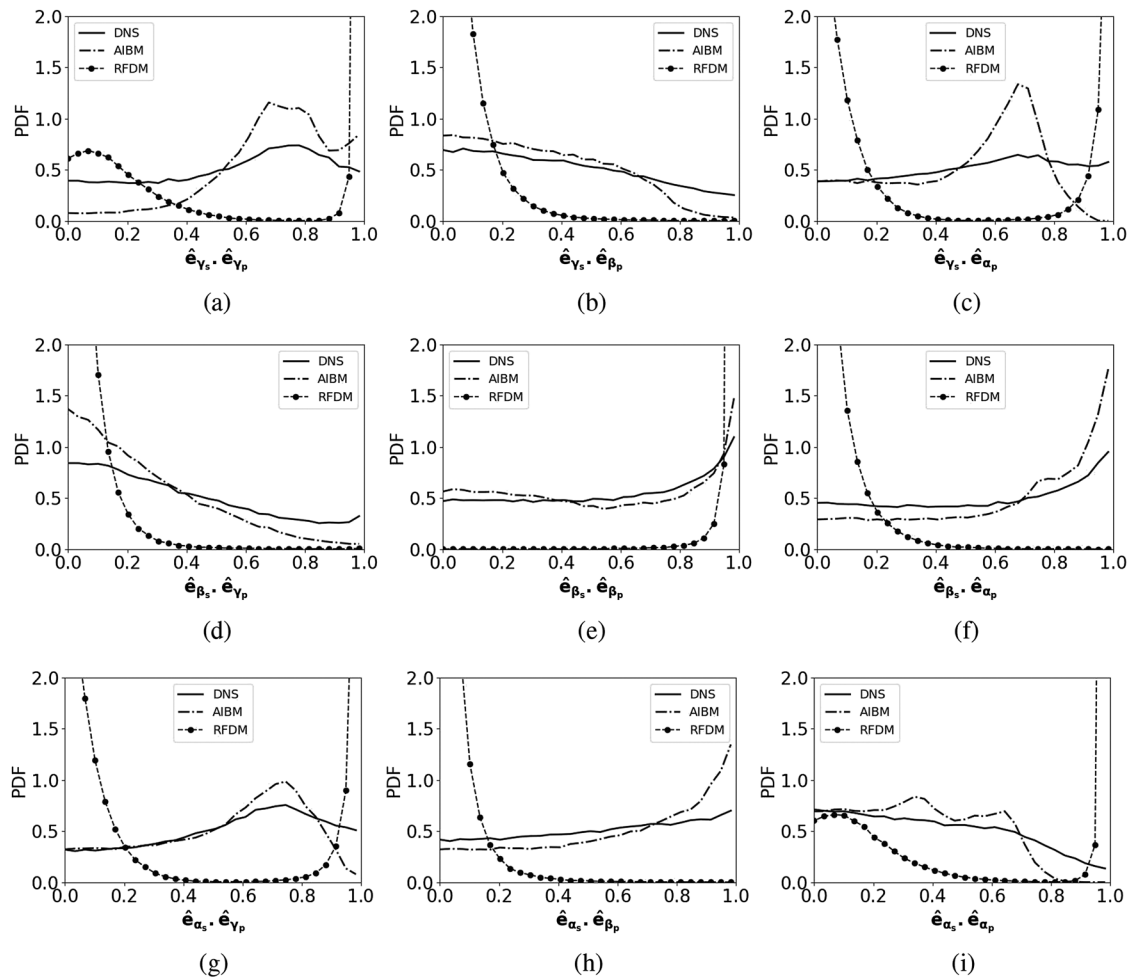


FIG. 9. PDFs of the cosine of the angle between the different eigenvectors of \mathbf{s} and those of $\hat{\mathbf{Q}}'$ in: (i) the DNS of isotropic incompressible turbulence²⁸ with $Re_\lambda = 433$, and (ii) the AIB model, and (iii) the RFD model.

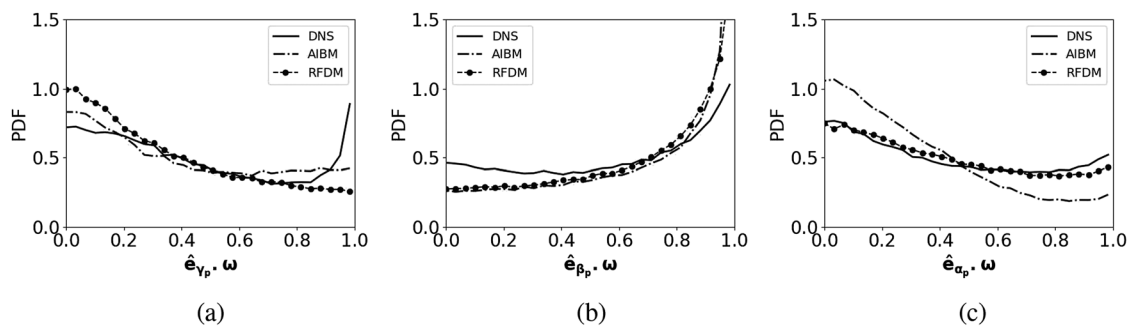


FIG. 10. PDFs of the cosine of the angle between the vorticity vector ($\boldsymbol{\omega}$) and the different eigenvectors of the anisotropic pressure Hessian tensor ($\hat{\mathbf{Q}}'$) in: (i) the DNS of isotropic incompressible turbulence²⁸ with $Re_\lambda = 433$, (ii) the AIB model, and (iii) the RFD model.

behavior seen in DNS. Furthermore, the RFD model shows a distribution close to the Dirac delta at $\psi = 0.10$. To quantify this comparison further, we have calculated the root mean square error (RMSE) between the model predictions (ψ_i^{model}) and the DNS results (ψ_i^{dns}),

$$RMSE = \sqrt{\frac{\sum_{i=0}^{i=n} (\psi_i^{dns} - \psi_i^{model})^2}{n}}, \quad (38)$$

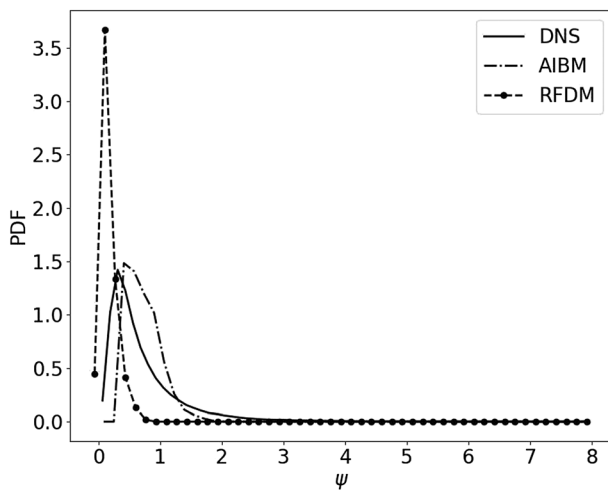


FIG. 11. PDF of ψ [Eq. (11)] in: (i) DNS of isotropic incompressible turbulence²⁸ with $Re_\lambda = 433$, (ii) the AIBM model, and (iii) the RFD model.

where n is the number of data points. Our calculations show that the RMSE in the AIBM case is 0.68, whereas that for the RFD case is 0.94. Thus, the relative improvement shown by AIBM compared to the RFD model is 28%, approximately.

To further evaluate the AIBM predictions of \mathbf{Q}' tensor, in Fig. 12, we present the plot of quantity ϕ [Eq. (31)] using the DNS data of source I. The DNS curve clearly shows that the magnitude of the anisotropic part does not vanish at small qe^2 values. In the same figure, we present predictions from the AIBM and the RFD model, as well. Both the models do capture the non-monotonous trend of the curve observed in DNS results with a non-vanishing ϕ at $qe^2 = 0$. However, the AIBM performance is significantly better than the RFD model as the AIBM predictions almost coincide with the DNS data. Furthermore, the RMSE [defined in Eq. (38)] of ϕ predicted from AIBM and RFD with respect to the DNS data is calculated as 0.01 and 0.09, respectively. Thus, the relative improvement of AIBM over the RFD model is 89%, approximately.

Next, we evaluate our model using the DNS data from source II (Table I). Like source I, this is a simulation of incompressible isotropic stationary turbulence. However, the Reynolds number is different than that in source I. The Reynolds number based on the Taylor microscale is 315. This database does not provide the pressure field information. However, Kalelkar¹⁸ has demonstrated that the alignment statistics of velocity gradient and pressure Hessian tensor is fairly independent of the Reynolds number. Therefore, we still refer to the DNS curves of source I for this comparison. The input to the AIB and RFD models, however, is sourced from source II.

Figure 13 presents the AIBM-based predictions of alignment tendencies of the pressure Hessian eigenvectors with those of the strain-rate tensor. The eigenvectors of the \mathbf{Q}' tensor with the local vorticity vector are presented in Fig. 14. On the same figures, we also present the alignment results of the DNS and the RFD model. From these figures, we observe that the AIBM predictions remain the same as the predictions we had in Figs. 9 and 10. In contrast, the RFD model shows significant differences compared to its own predictions when the

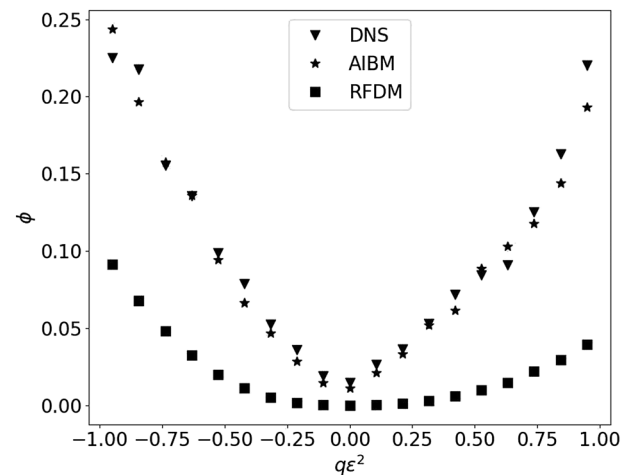


FIG. 12. Plot of ϕ [Eq. (31)] vs qe^2 in: (i) DNS of isotropic incompressible turbulence²⁸ with $Re_\lambda = 433$, (ii) the AIBM model, and (iii) the RFD model.

source I data were used to provide input to the model. Based on these results, we conclude that the AIBM predictions of alignments of the pressure Hessian eigenvectors with the strain-rate eigenvectors and the local vorticity vector are independent of the Taylor Reynolds number (at least over the range studied in this work). In contrast, the RFD results of the pressure Hessian and strain rate tensor alignment tendencies show a clear dependence on the Reynolds number, which is not in line with the known turbulence behavior.¹⁸

B. Channel flow

In this subsection, we present the evaluations of AIBM in the channel flow field. In Fig. 15, we present the AIBM predictions of the alignment tendencies of the eigen-vectors of \mathbf{Q}' tensor relative to those of the local strain rate tensor (\mathbf{s}). Figure 16 shows the alignment tendencies of \mathbf{Q}' tensor with the local vorticity vector ($\boldsymbol{\omega}$). For comparisons, the results from the DNS and the RFD model are also presented in the same figures. We observe that the DNS alignments of the pressure Hessian tensor, along with the strain rate tensor and the local vorticity vector, show similar trends as those of the isotropic turbulent flows (refer to Figs. 9 and 10). Qualitatively, AIBM also shows a behavior similar to the channel flow DNS (except in some alignment PDFs, the peaks are of slightly higher magnitude than the DNS peaks). In contrast, the RFD model results are significantly different than the DNS behavior.

The PDFs of ψ computed from AIBM, RFD, and the channel flow DNS database (source III) are presented in Fig. 17. We observe that the DNS curve has a wide range (0,33). However, the probability of fluid particles with $\psi > 8$ is nearly zero. Furthermore, the DNS plot shows a single peak at $\psi = 0.31$. The RFD model fails to capture the distribution width as observed in DNS. Also, the RFD model shows a distribution being close to the Dirac delta at $\psi = 0.13$. In contrast, the AIBM captures the width of the DNS distribution reasonably well, having a peak at $\psi = 0.41$. The magnitude of PDF peak in the case of AIBM is somewhat greater than the DNS curve peak. In contrast, the RFD model shows its PDF peak with a significantly higher magnitude (greater than 2). The RMSE [defined in Eq. (38)] of ψ predicted from

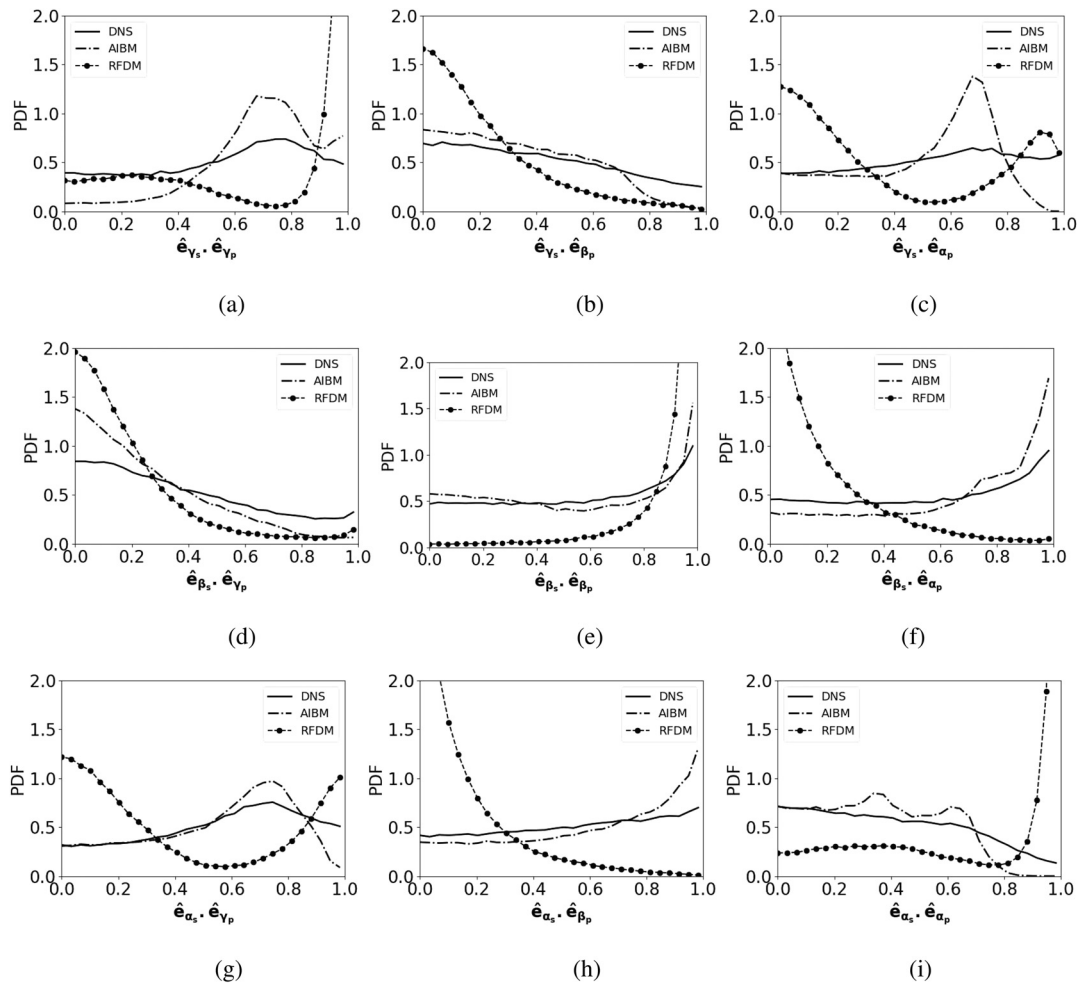


FIG. 13. PDFs of the cosine of the angle between the different eigenvectors of \mathbf{s} and those of $\hat{\mathbf{Q}}'$ in: (i) the DNS of isotropic incompressible turbulence⁴³ with $Re_\lambda = 315$, (ii) the AIB model, and (iii) the RFD model.

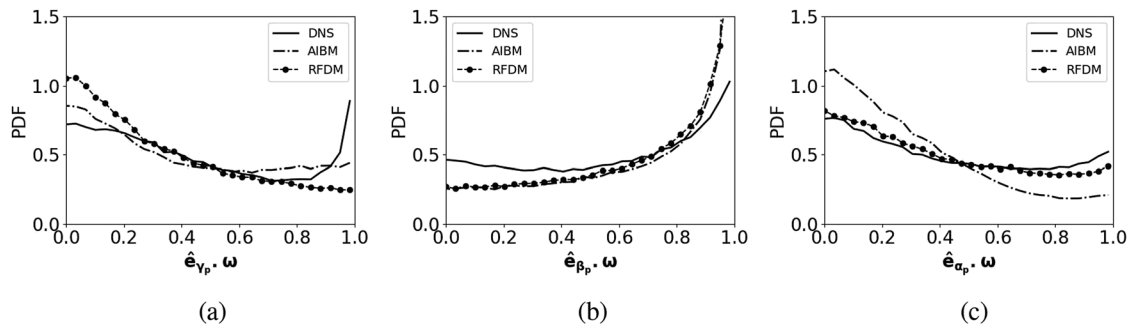


FIG. 14. PDFs of the cosine of the angle between the vorticity vector (ω) and the different eigenvectors of the anisotropic pressure Hessian tensor ($\hat{\mathbf{Q}}'$) in: (i) DNS of isotropic incompressible turbulence⁴³ with $Re_\lambda = 315$, (ii) the AIB model, and (iii) the RFD model.

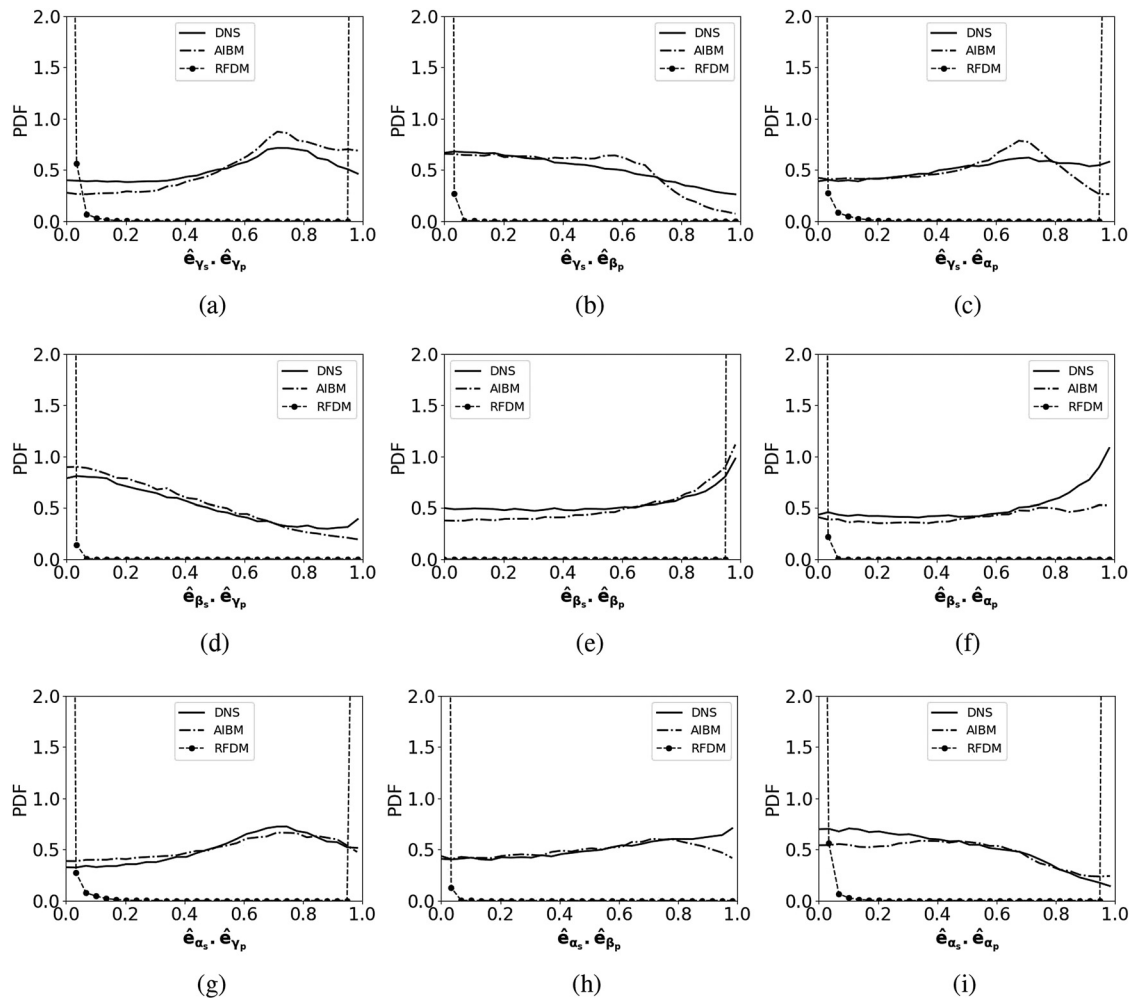


FIG. 15. PDFs of the cosine of the angle between the different eigenvectors of \mathbf{s} and those of $\hat{\mathbf{Q}}^f$ in: (i) DNS data of channel flows,³⁷ (ii) the AIBM model, and (iii) the RFD model.

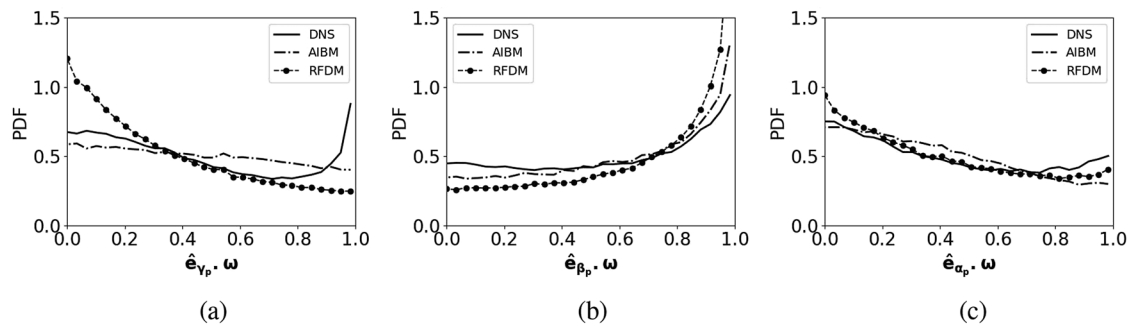


FIG. 16. PDFs of the cosine of the angle between the vorticity vector (ω) and the different eigenvectors of the anisotropic pressure Hessian tensor ($\hat{\mathbf{Q}}^f$) in: (i) DNS data of channel flows,³⁷ (ii) the AIBM model, and (iii) the RFD model.

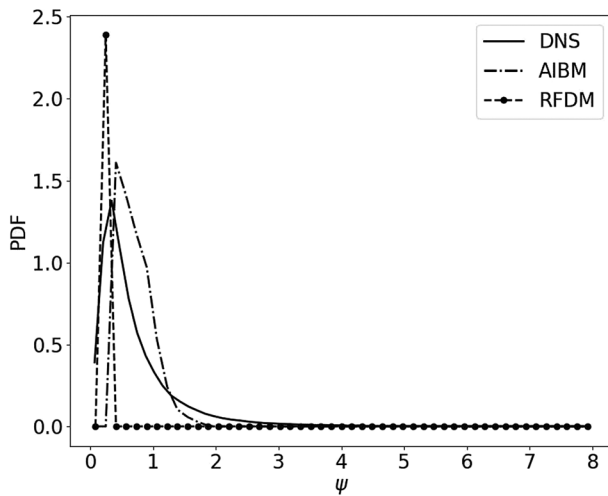


FIG. 17. PDF of ψ [Eq. (11)] in: (i) DNS data of channel flows,³⁷ (ii) the AIB model, and (iii) the RFD model.

AIBM and RFD with respect to the DNS data of channel flows is calculated as 0.69 and 1.03, respectively. Thus, the relative improvement of AIBM over RFD is 33%, approximately.

In Fig. 18, we present the AIBM predictions of ϕ [Eq. (31)]. A comparison of the reference DNS results and the RFD model results are also presented in the same figure. We observe that the AIBM predictions are close to DNS results in the nearby region of $qe^2 = 0$. However, it deteriorates in the region of $-0.5 > qe^2 > 0.5$. Like stationary isotropic turbulence (Fig. 12), the DNS results show a non-monotonous trend with the essential feature of having a non-vanishing ϕ value at $qe^2 = 0$. This trend is captured by AIBM. The RFD model shows gross disagreement. The RMSE [defined in Eq. (38)] of ϕ predicted from AIBM and RFD with respect to the DNS data of channel flows is calculated as 0.05 and 0.12, respectively.

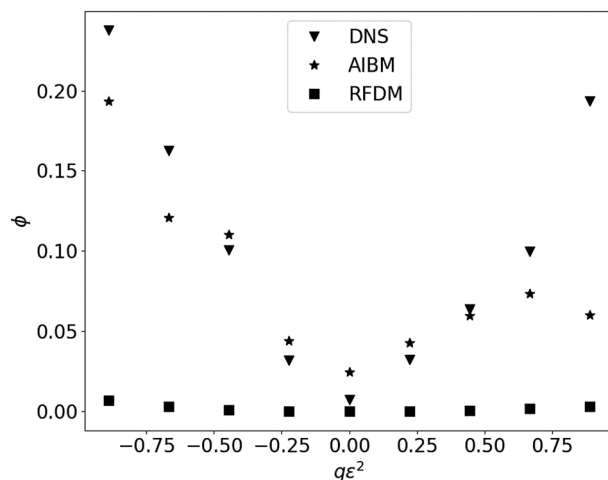


FIG. 18. Plot of ϕ [Eq. (31)] vs qe^2 in: (i) DNS data of channel flows,³⁷ (ii) the AIB model, and (iii) the RFD model.

Evidently, the AIBM performs significantly better than the RFD model (relative improvement of 58%, approximately).

The RFD model was originally developed for incompressible isotropic stationary turbulent flows at $Re_\lambda = 150$. Based on the comparisons done for incompressible flows, we observe that the performance of this model differs significantly from the DNS results when tested for different Reynolds numbers ($Re_\lambda = 433$ and 315) even in isotropic stationary turbulent flows. This drawback of model has been acknowledged by the authors themselves in Chevillard *et al.*¹³ Moreover, the performance of the RFD model further deteriorates when tested for a different kind of flow (channel flow).

C. Compressible isotropic turbulence

The nature of pressure evolution in a compressible flow field is different compared to a strictly incompressible flow field, wherein pressure depends entirely on the velocity field through Poisson's equation [Eq. (6)]. In a compressible medium, pressure behaves like a thermodynamic variable. With its dependence on the local density and temperature, the evolution of pressure, and, in turn, that of the pressure Hessian, physics becomes coupled with the continuity and energy equations. Thus, the influence of pressure on the velocity gradient dynamics of compressible turbulence is no longer controlled entirely by the velocity field. Furthermore, the existence of non-zero density gradients leads to the appearance of an altogether new process affecting the velocity gradients. The evolution equation of A_{ij} in a compressible medium is as follows:

$$\frac{dA_{ij}}{dt} = -A_{ik}A_{kj} - H_{ij} + B_{ij} + \Gamma_{ij}, \quad (39)$$

where

$$H_{ij} = \frac{1}{\rho} \frac{\partial^2 p}{\partial x_i \partial x_j}, \quad B_{ij} = \frac{1}{\rho^2} \frac{\partial p}{\partial x_i} \frac{\partial \rho}{\partial x_j}, \quad \Gamma_{ij} = \frac{\partial}{\partial x_j} \left[\frac{1}{\rho} \frac{\partial \sigma_{ik}}{\partial x_k} \right],$$

where σ_{ik} represents viscous stress tensor. Equation (39) clearly shows that besides the second gradient of pressure (the pressure Hessian), the first gradient of pressure and that of density interact to further influence the velocity gradients in a compressible flow field. The first process is at least algebraically identical to the pressure Hessian process identified in incompressible turbulence [Eq. (3)]. In contrast, the second process involves the cross-product of density gradients and pressure gradients. This process can be called the baroclinic process in the evolution of velocity gradients.

Despite these additional complexities existing in a compressible flow field, Suman and Girimaji⁹ report that appropriately conditioned statistics of some quantities, even in compressible turbulence, are quite similar to those seen in incompressible turbulence. Such conditioning is done based on two local compressibility parameters. The first compressibility parameter is defined as the locally normalized version of the dilatation rate

$$a_{ii} = \frac{A_{ii}}{\sqrt{A_{mn}A_{mn}}}. \quad (40)$$

The second compressibility parameter is defined as follows:

$$\delta = \frac{-A_{ij}A_{ji} - H_{ii} + B_{ii}}{\varepsilon^2}, \quad (41)$$

where ε is the magnitude of the local velocity gradient tensor [Eq. (8)].

The significance of the locally normalized dilatation rate can be highlighted with respect to an appropriately normalized version of the continuity equation⁹

$$\frac{d\rho}{\rho dt'} = -a_{ii}, \quad (42)$$

where $dt' = \varepsilon dt$. A positive value of a_{ii} implies an instantaneously expanding fluid element, whereas a negative value of a_{ii} implies a contracting fluid element. An instantaneously volume-preserving fluid element would have $a_{ii} = 0$.

To highlight the significance of δ , we consider the trace of Eq. (39)

$$\frac{dA_{ii}}{dt} = -A_{ik}A_{ki} - H_{ii} + B_{ii} + \Gamma_{ii}. \quad (43)$$

This equation is re-cast in its normalized form as

$$\frac{1}{\varepsilon} \frac{dA_{ii}}{dt'} = -\frac{A_{ik}A_{ki}}{\varepsilon^2} - \frac{H_{ii}}{\varepsilon^2} + \frac{B_{ii}}{\varepsilon^2} + \frac{\Gamma_{ii}}{\varepsilon^2}. \quad (44)$$

Comparing the inviscid processes on the RHS of Eq. (44) with the definition of δ in Eq. (41), it is clear that δ represents the local imbalance between the self-stretching process and the influence of thermodynamics on the dynamics of the dilatation rate (A_{ii}).

Equations (42) and (44) clearly suggest that while a_{ii} determines how fast the density of a local fluid element is changing, δ indicates how fast the dilatation rate itself changes due to the inviscid processes. Suman and Girimaji⁹ show that even in flow fields with high turbulent Mach number, the statistics of velocity gradients when conditioned on those fluid elements that are instantaneously volume preserving are quite similar to the statistics observed in incompressible turbulence. Furthermore, they demonstrate that the statistics related to the pressure Hessian tensor in compressible turbulence, when double conditioned on those fluid elements that have $a_{ii} \approx 0$ and $\delta \approx 0$, are very similar to those seen in incompressible turbulence. These statistics include (i) the alignment of the vorticity vector with the eigenvectors of the pressure Hessian tensor and (ii) the alignment of the eigenvectors of the pressure Hessian tensor with those of the local strain-rate tensor. These observations hold significance, especially, in light of the fact that even in flow fields with high turbulent Mach numbers, the majority of the fluid elements still have $a_{ii} \approx 0$ and $\delta \approx 0$. Suman and Girimaji⁹ show probability density functions of a_{ii} and δ from several simulations of compressible decaying turbulence and demonstrate that, indeed, these PDFs show distinct single peaks at $a_{ii} \approx 0$.

The AIB model for the anisotropic part of the pressure Hessian tensor we have developed to capture the essential orientations of the eigenvector directions is actually based on the physical behavior of incompressible turbulence, wherein all fluid elements have $a_{ii} = 0$ and $\delta = 0$ at all times. Thus, it is not reasonable to expect AIBM to unconditionally recover the behavior of compressible turbulence for all constituent fluid elements existing in such flow fields. However, in light of the findings of Suman and Girimaji,⁹ it is still plausible to perform, up to a limited extent, the evaluation of our AIBM in compressible flows. We evaluate the performance of the model restricting to at least those

fluid elements of a compressible flow field, which have instantaneous $a_{ii} \approx 0$ and $\delta \approx 0$.

For this evaluation, we employ an available DNS database of compressible decaying turbulence (source IV, Table I). This database has earlier been used by Suman and Girimaji⁹ to perform various studies on compressible velocity gradient dynamics. This simulation has been performed over a cuboidal computational domain with periodic boundary conditions imposed on the opposite faces. The initial turbulent Mach number and the initial Reynolds number based on the Taylor microscale are 1.2 and 55.6, respectively. For further details about these simulations, the reader is referred to Kumar *et al.*⁴⁴

Using this DNS database from source IV (Table I), we first extract the velocity and the thermodynamic (pressure, density, and temperature) fields at a time instant when the dissipation has reached its peak, and thus, the non-linear processes are in full effect. Using this flow field, the required gradients are computed using fourth-order accurate finite difference schemes. Subsequently, we select only those fluid elements that have their a_{ii} and δ approximately zero. Using this conditioned sample, we then compute the required statistics of velocity gradient and the pressure Hessian tensors. The velocity gradient tensor thus obtained is used as input to predict the behavior of the anisotropic pressure Hessian tensor using the AIB model. The predicted behavior from the model is then compared with the statistics of pressure Hessian obtained directly from the DNS flow field of source IV.

In Fig. 19, we present the AIBM predictions of the alignment tendencies of the eigen-vectors of the $\hat{\mathbf{Q}}$ tensor relative to those of the local strain rate tensor (\mathbf{s}). Figure 20 shows the alignment tendencies of $\hat{\mathbf{Q}}$ tensor with the local vorticity vector ($\boldsymbol{\omega}$). For comparisons, the results from the DNS database are also presented on these same figures. We observe that the double-conditioned DNS data of compressible flows show similar alignment trends as those of the strictly incompressible flows (refer Figs. 9 and 10). Furthermore, the AIBM predictions show a good agreement with the DNS curves except for the PDF of $\hat{\mathbf{e}}_{\beta_p} \cdot \hat{\mathbf{e}}_{\gamma_s}$ and $\hat{\mathbf{e}}_{\beta_p} \cdot \hat{\mathbf{e}}_{\alpha_s}$ for which the model shows peak near 0.7, which are different than the DNS data peaks. In DNS results, the peaks of $\hat{\mathbf{e}}_{\beta_p} \cdot \hat{\mathbf{e}}_{\gamma_s}$ and $\hat{\mathbf{e}}_{\beta_p} \cdot \hat{\mathbf{e}}_{\alpha_s}$ PDFs are at 0 and 1, respectively. Based on these results, we conclude that the AIBM captures most of the trends observed in DNS.

In Fig. 21, we present the PDF of ψ [Eq. (11)] using the conditioned compressible DNS data. We also present the AIBM predictions in the same figure. Compared to the strictly incompressible DNS results (refer Fig. 11), the conditioned compressible DNS curve is narrower and has a peak at $\psi = 0.18$ with higher value of the PDF. AIBM indeed adapts to this change (compare the Figs. 11 and 21). In Fig. 21, the AIBM shows the peak at $\psi = 0.41$, with the same value of PDF as that of the DNS curve.

Based on the above results, we conclude that the ML-based model (AIBM) proposed in this work does recover some known conditional behavior of pressure Hessian alignment and magnitude tendencies even in compressible turbulence for fluid elements, which have $a_{ii} \approx 0$ and $\delta \approx 0$. For other fluid elements that have non-zero a_{ii} and non-zero δ , the current model is neither applicable nor sensible to be evaluated at this point. However, the presented results show the promise of the proposed methodology based on two separate neural networks to capture the alignment tendencies, as well as the magnitude of the anisotropic pressure Hessian tensor. For compressible flows, further research efforts are still required. These efforts must explore advancing

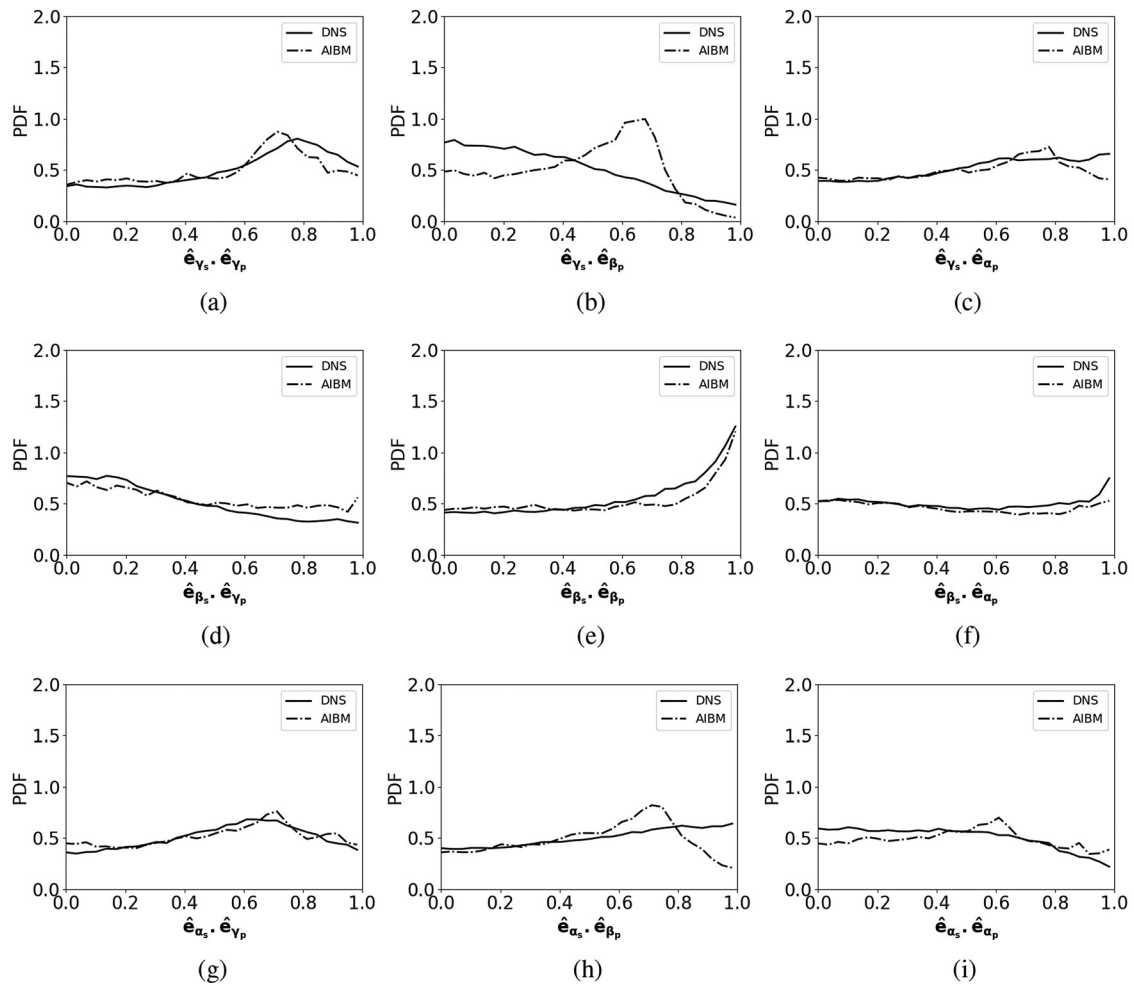


FIG. 19. PDFs of the cosine of the angle between the different eigenvectors of \mathbf{s} and those of $\hat{\mathbf{Q}}'$ in: (i) DNS of compressible isotropic decaying turbulence⁴⁴ jointly conditioned on $a_{ij} \approx 0$ and $\delta \approx 0$, and (ii) the AIBM model.

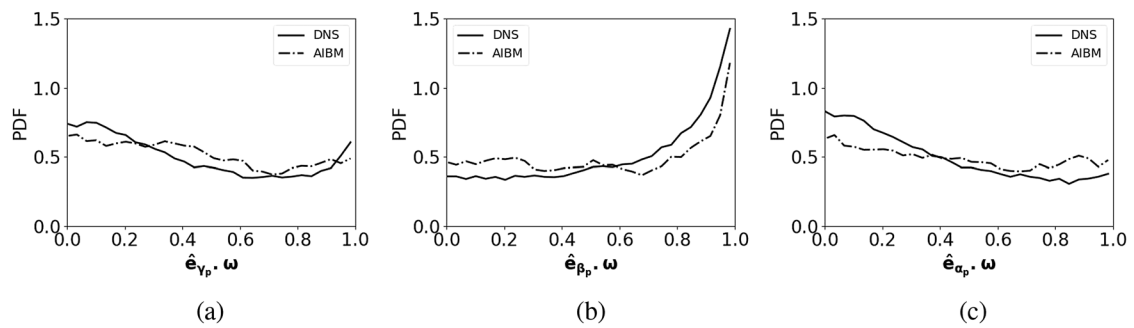


FIG. 20. PDFs of the cosine of the angle between the vorticity vector (ω) and the different eigenvectors of the anisotropic pressure Hessian tensor ($\hat{\mathbf{Q}}'$) in: (i) DNS of compressible isotropic decaying turbulence⁴⁴ jointly conditioned on $a_{ij} \approx 0$ and $\delta \approx 0$, and (ii) the AIBM model.

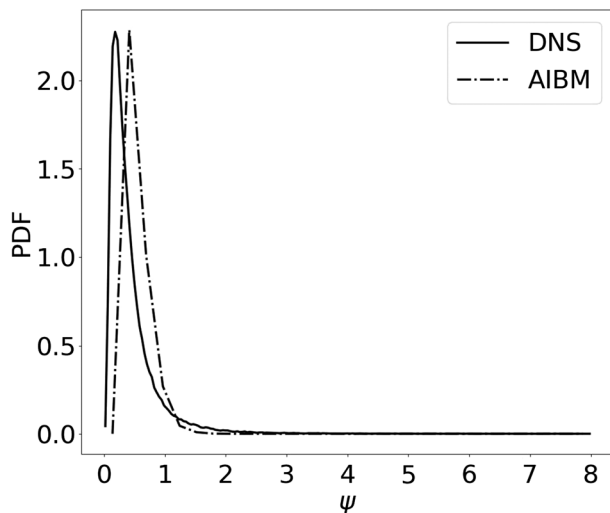


FIG. 21. PDF of ψ in: (i) DNS of compressible isotropic decaying turbulence⁴⁴ jointly conditioned on $a_{ii} \approx 0$ and $\delta \approx 0$, and (ii) the AIBM model.

the proposed neural networks of AIBM to accept inputs also from those fluid elements that have non-zero dilatation. Accordingly, the basis tensors may need to be aptly modified. Furthermore, the physics of the baroclinic process highlighted in Eq. (39) may need to be examined more closely and aptly modeled. Even though these endeavors are outside the scope of the current work; such will be the focus of our future studies.

VII. CONCLUSIONS

Computing the evolution of velocity gradients following individual fluid elements is a viable approach to examine and understand many non-linear turbulence processes of interest. However, the pressure Hessian tensor is one of the mathematically unclosed terms in the evolution equation of the velocity gradient tensor. Several researchers have attempted modeling this tensor using various phenomenological approaches.

In this work, using machine-learning (ML) tools, we introduce two novel advancements toward developing an advanced model of the pressure Hessian tensor (i) we use a combination of two different neural networks to separately predict the magnitude and the eigenvector alignments of the pressure Hessian tensor, and (ii) we use mathematically optimal and physics-assisted customized loss functions separately for the two aspects (alignment and magnitude) of the predicted second-order tensor. The input parameters of the second neural network are carefully chosen based on a DNS-based study on the behavior of the magnitude of the pressure Hessian tensor (Sec. III B). We refer to the new model as the augmented invariant-based model (AIBM) for the pressure Hessian tensor.

The two networks are trained separately using the same common flow field having stationary homogeneous isotropic incompressible turbulence. Subsequently, an extensive evaluation of the model is performed using direct numerical simulation (DNS) flow fields of not only isotropic turbulence at different Reynolds numbers but also using DNS flow fields of incompressible channel flow and compressible decaying isotropic turbulence. To clearly demonstrate the superiority

of the new model compared to existing phenomenological models of the pressure Hessian tensor, we perform direct comparisons with the predictions of the so-called recent fluid deformation closure (RFD) model, which is indeed considered to be the most-advanced phenomenological model of the pressure Hessian tensor in contemporary literature.

We perform model evaluations in terms of both the structural (relative orientations of the eigenvectors of the pressure Hessian tensor with those of the local strain-rate tensors) and the magnitude of the tensor. We demonstrate that the AIBM consistently recovers various turbulence statistics in all the flow fields considered in this work. Completely in line with the known turbulence behavior, the model shows robustness in capturing the near-universal orientation tendencies of the eigenvector of the pressure Hessian tensor at different Reynolds numbers and in different types of the flow field. On the other hand, the model shows the capability to adapt and predict the magnitude-related aspects of the tensor, which are observed to be changing in different DNS flow fields. We demonstrate that the AIBM performance is superior to that of the RFD model in several ways:

1. In homogeneous isotropic incompressible turbulent flow field, the AIBM model captures the probability density functions of the cosine of the angle between the eigenvectors of the pressure Hessian tensor and those of the local strain-rate tensor much better than what is observed in the predictions of the RFD model (Figs. 9 and 13). The AIBM demonstrates that its prediction of the alignment tendencies, like in DNS, is fairly independent of the Reynolds number (Figs. 9 vs 13). In contrast, the predictions of the RFD model change significantly as the Reynolds number changes.
2. In homogeneous isotropic incompressible turbulent flow fields, the AIBM captures the statistics of the magnitude of the pressure Hessian tensor quite well compared to the RFD model as evident in Figs. 11 and 12.
3. In the channel flow field, which is a representative inhomogeneous turbulent flow field (which is not only a different type of the flow field than the flow in which the AIBM was trained, but its Reynolds number is also quite different), the AIBM model still captures the alignment tendencies of the pressure Hessian eigenvectors and those of the local strain-rate eigenvectors quite well when compared to the behavior observed in the DNS database as evident in Fig. 15. In contrast, the performance of the RFD model is quite inferior.
4. In terms of the statistics of the magnitude of the pressure Hessian tensor in the channel flow field, the predictions of the AIBM are close to that observed in DNS. In contrast, the predictions of the RFD model are significantly different from the DNS results (Figs. 17 and 18).

We have evaluated the performance of the new model even in compressible flow fields, wherein the evaluation is performed on a set of appropriately conditioned fluid particles. Even though in compressible flows the agreement between the model predictions and the DNS behavior is not as good as it is in incompressible flow fields, the model predictions still capture the essential flow features quite well (Figs. 19–21).

Based on these evaluations, we conclude that the new methodology of using two separate neural networks for modeling the alignment

and the magnitude of the pressure Hessian tensor seems to be a robust and potent method for incompressible turbulent flows and can possibly be further enhanced to predict the pressure Hessian behavior in compressible flows, as well.

ACKNOWLEDGMENTS

This work has been supported by the Science and Engineering Research Board (SERB), Department of Science and Technology, Government of India through Project No. CRG/2022/002378. The high-performance computing resource required for this work has been made available by the High-Performance Computing Center (HPC), Indian Institute of Technology Delhi, India.

AUTHOR DECLARATIONS

Conflict of Interest

The authors have no conflicts to disclose.

Author Contributions

Deep Shikha: Conceptualization (equal); Formal analysis (equal).
Sawan S. Sinha: Supervision (equal); Writing – review & editing (equal).

DATA AVAILABILITY

The data that support the findings of this study are available from the corresponding author upon reasonable request.

REFERENCES

- ¹P. Vieillefosse, "Local interaction between vorticity and shear in a perfect incompressible fluid," *J. Phys.* **43**, 837–842 (1982).
- ²W. T. Ashurst, A. Kerstein, R. Kerr, and C. Gibson, "Alignment of vorticity and scalar gradient with strain rate in simulated Navier–Stokes turbulence," *Phys. Fluids* **30**, 2343–2353 (1987).
- ³S. Girimaji and S. Pope, "Material-element deformation in isotropic turbulence," *J. Fluid Mech.* **220**, 427–458 (1990).
- ⁴K. Ohkitani, "Eigenvalue problems in three-dimensional Euler flows," *Phys. Fluids A* **5**, 2570–2572 (1993).
- ⁵K. Ohkitani and S. Kishiba, "Nonlocal nature of vortex stretching in an inviscid fluid," *Phys. Fluids* **7**, 411–421 (1995).
- ⁶H. Xu, A. Pumir, and E. Bodenschatz, "The pirouette effect in turbulent flows," *Nat. Phys.* **7**, 709–712 (2011).
- ⁷S. Suman and S. Girimaji, "Dynamical model for velocity-gradient evolution in compressible turbulence," *J. Fluid Mech.* **683**, 289–319 (2011).
- ⁸M. Danish, S. Suman, and B. Srinivasan, "A direct numerical simulation-based investigation and modeling of pressure hessian effects on compressible velocity gradient dynamics," *Phys. Fluids* **26**, 126103 (2014).
- ⁹S. Suman and S. S. Girimaji, "Velocity gradient dynamics in compressible turbulence: Characterization of pressure-Hessian tensor," *Phys. Fluids* **25**, 125103 (2013).
- ¹⁰N. Parashar, S. S. Sinha, and B. Srinivasan, "Lagrangian investigations of velocity gradients in compressible turbulence: Lifetime of flow-field topologies," *J. Fluid Mech.* **872**, 492–514 (2019).
- ¹¹B. J. Cantwell, "Exact solution of a restricted Euler equation for the velocity gradient tensor," *Phys. Fluids A* **4**, 782–793 (1992).
- ¹²E. Jeong and S. S. Girimaji, "Velocity-gradient dynamics in turbulence: Effect of viscosity and forcing," *Theor. Comput. Fluid Dyn.* **16**, 421–432 (2003).
- ¹³L. Chevillard, C. Meneveau, L. Biferale, and F. Toschi, "Modeling the pressure Hessian and viscous Laplacian in turbulence: Comparisons with direct numerical simulation and implications on velocity gradient dynamics," *Phys. Fluids* **20**, 101504 (2008).
- ¹⁴S. Suman and S. Girimaji, "Homogenized Euler equation: A model for compressible velocity gradient dynamics," *J. Fluid Mech.* **620**, 177–194 (2009).
- ¹⁵S. B. Pope, "Pdf methods for turbulent reactive flows," *Prog. Energy Combust. Sci.* **11**, 119–192 (1985).
- ¹⁶J. Martin, A. Ooi, C. Dopazo, M. S. Chong, and J. Soria, "The inverse diffusion time scale of velocity gradients in homogeneous isotropic turbulence," *Phys. Fluids* **9**, 814–816 (1997).
- ¹⁷N. Parashar, B. Srinivasan, and S. S. Sinha, "Modeling the pressure-hessian tensor using deep neural networks," *Phys. Rev. Fluids* **5**, 114604 (2020).
- ¹⁸C. Kalelkar, "Statistics of pressure fluctuations in decaying isotropic turbulence," *Phys. Rev. E* **73**, 046301 (2006).
- ¹⁹L. Chevillard and C. Meneveau, "Lagrangian dynamics and statistical geometric structure of turbulence," *Phys. Rev. Lett.* **97**, 174501 (2006).
- ²⁰S. Brunton, B. Noack, and P. Koumoutsakos, "Machine learning for fluid mechanics," *arXiv:1905.11075* (2019).
- ²¹R. Maulik, O. San, A. Rasheed, and P. Vedula, "Subgrid modelling for two-dimensional turbulence using neural networks," *J. Fluid Mech.* **858**, 122–144 (2019).
- ²²X. Jin, S. Cai, H. Li, and G. E. Karniadakis, "NSfnets (Navier–Stokes flow nets): Physics-informed neural networks for the incompressible Navier–Stokes equations," *J. Comput. Phys.* **426**, 109951 (2021).
- ²³B. Liu, J. Tang, H. Huang, and X.-Y. Lu, "Deep learning methods for super-resolution reconstruction of turbulent flows," *Phys. Fluids* **32**, 025105 (2020).
- ²⁴J. Ling, A. Kurawski, and J. Templeton, "Reynolds averaged turbulence modelling using deep neural networks with embedded invariance," *J. Fluid Mech.* **807**, 155–166 (2016).
- ²⁵S. Pope, "A more general effective-viscosity hypothesis," *J. Fluid Mech.* **72**, 331–340 (1975).
- ²⁶I. Goodfellow, Y. Bengio, and A. Courville, *Deep Learning* (MIT Press, 2016).
- ²⁷M. E. Rose, *Elementary Theory of Angular Momentum* (Courier Corporation, 1995).
- ²⁸Y. Li, E. Perlman, M. Wan, Y. Yang, C. Meneveau, R. Burns, S. Chen, A. Szalay, and G. Eyink, "A public turbulence database cluster and applications to study Lagrangian evolution of velocity increments in turbulence," *J. Turbul.* **9**, N31 (2008).
- ²⁹J. Snoek, H. Larochelle, and R. P. Adams, "Practical Bayesian optimization of machine learning algorithms," *Adv. Neural Inf. Process. Syst.* **2**, 2951 (2012).
- ³⁰N. Srivastava, G. Hinton, A. Krizhevsky, I. Sutskever, and R. Salakhutdinov, "Dropout: A simple way to prevent neural networks from overfitting," *J. Mach. Learn. Res.* **15**, 1929–1958 (2014).
- ³¹M. S. Chong, A. E. Perry, and B. J. Cantwell, "A general classification of three-dimensional flow fields," *Phys. Fluids A* **2**, 765–777 (1990).
- ³²P. O'Neill and J. Soria, "The relationship between the topological structures in turbulent flow and the distribution of a passive scalar with an imposed mean gradient," *Fluid Dyn. Res.* **36**, 107 (2005).
- ³³J. Soria, R. Sondergaard, B. Cantwell, M. Chong, and A. Perry, "A study of the fine-scale motions of incompressible time-developing mixing layers," *Phys. Fluids* **6**, 871–884 (1994).
- ³⁴O. N. Boratav and R. B. Pelz, "On the local topology evolution of a high-symmetry flow," *Phys. Fluids* **7**, 1712–1731 (1995).
- ³⁵J. M. Chacín, B. J. Cantwell, and S. J. Kline, "Study of turbulent boundary layer structure using the invariants of the velocity gradient tensor," *Exp. Therm. Fluid Sci.* **13**, 308–317 (1996).
- ³⁶H. M. Blackburn, N. N. Mansour, and B. J. Cantwell, "Topology of fine-scale motions in turbulent channel flow," *J. Fluid Mech.* **310**, 269–292 (1996).
- ³⁷J. Graham, K. Kanov, X. Yang, M. Lee, N. Malaya, C. Lalescu, R. Burns, G. Eyink, A. Szalay, R. Moser *et al.*, "A web services accessible database of turbulent channel flow and its use for testing a new integral wall model for les," *J. Turbul.* **17**, 181–215 (2016).
- ³⁸S. B. Pope and S. B. Pope, *Turbulent Flows* (Cambridge University Press, 2000), p. 198.
- ³⁹S. B. Pope and S. B. Pope, *Turbulent Flows* (Cambridge University Press, 2000), p. 270.
- ⁴⁰K. Duraisamy, G. Iaccarino, and H. Xiao, "Turbulence modeling in the age of data," *Annu. Rev. Fluid Mech.* **51**, 357–377 (2019).

- ⁴¹Y. Zhou, "Turbulence theories and statistical closure approaches," *Phys. Rep.* **935**, 1–117 (2021).
- ⁴²A. Tozzi, "The multidimensional brain," *Phys. Life Rev.* **31**, 86–103 (2019).
- ⁴³J. I. Cardesa, A. Vela-Martín, and J. Jiménez, "The turbulent cascade in five dimensions," *Science* **357**, 782–784 (2017).
- ⁴⁴G. Kumar, S. S. Girimaji, and J. Kerimo, "WENO-enhanced gas-kinetic scheme for direct simulations of compressible transition and turbulence," *J. Comput. Phys.* **234**, 499–523 (2013).
- ⁴⁵J. Ling, R. Jones, and J. Templeton, "Machine learning strategies for systems with invariance properties," *J. Comput. Phys.* **318**, 22–35 (2016).